Coronal Mass Ejections: a Summary of Recent Results

N. Gopalswamy, NASA Goddard Space Flight Center, Greenbelt, MD 20771, USA, nat.gopalswamy @nasa.gov

Abstract

Coronal mass ejections (CMEs) have been recognized as the most energetic phenomenon in the heliosphere, deriving their energy from the stressed magnetic fields on the Sun. This paper summarizes the properties of CMEs and highlights some of the recent results on CMEs. In particular, the morphological, physical, and kinematic properties of CMEs are summarized. The CME consequences in the heliosphere such as interplanetary shocks, type II radio bursts, energetic particles, geomagnetic storms, and cosmic ray modulation are discussed.

1. Introduction

A coronal mass ejection (CME) can be defined as a concentrated material in the corona moving away from the Sun, but distinct from the solar wind. In coronagraphic images, a CME can be recognized as bright features moving to progressively larger heliocentric distances. The movement is such that the lower part of the feature is always connected to the Sun, i.e., the CME is anchored to the Sun and it expands into the interplanetary space. The outward motion implies a finite speed of the CMEs and the motion from rest implies acceleration. The CME occupies a portion of the coronal images indicating a finite angular extent and hence defines a finite quantity of matter expelled from the Sun. CMEs are ejected into the ambient medium, which expands as the solar wind. The CMEs and the solar wind are supposed to exchange momentum. If a CME moves faster than the characteristic speed of the ambient medium, it can drive a shock which have additional consequences.

The CME phenomenon was discovered only in 1971 (Tousey, 1973), but has become the most important form of solar activity being studied by many research groups because it is the most energetic phenomena on the Sun with a wide-ranging influence throughout the heliosphere. Great advances have been made in understanding CMEs after the advent of the coronagraphs on board the Solar and Heliospheric Observatory (SOHO). In addition, space missions such as Wind, Advanced Composition Explorer (ACE), and Ulysses have provided complementary information on the interplanetary manifestation of CMEs. Finally, the Solar Terrestrial Relations Observatory (STEREO) provided some crucial confirmation on the 3D nature of CMEs. This paper provides an overview of the knowledge gained over the past decade, with a heavy bias to the work done by the author's group. The paper is organized as follows:

Section 2 describes the basic properties of CMEs, covering the morphological, physical, kinematic, and source properties. Section 3 discusses halo CMEs, which is a special population of CMEs having wide ranging consequences in the heliosphere. Section 4 describes various properties of CME-driven shocks including their ability to produce type II radio bursts. Section 5 describes the connection between coronal and IP manifestations of CMEs. Section 6 summarizes the three major consequences of CMEs in the heliosphere: cosmic ray modulation, geomagnetic storms and solar energetic particles. A summary is given in section 7.

2. CME Properties

2.1 Morphological Properties

Figure 1 illustrates a CME observed by SOHO's Large Angle and Spectrometric Coronagraph (LASCO). LASCO employs an occulting disk (marked OD) to block the bright photospheric light so the faint coronal structures can be observed better. The structures are bright because the electrons contained in them scatter the photospheric light through a process known as Thomson scattering. One can recognize two types of bright features in the images: the CME and several elongated features which are coronal streamers. In frame 1, the CME can be seen just above the occulting disk. The structure actually goes close to the solar surface (represented by the white circle overlaid on the occulting disk). In frame 2, taken about an hour after frame 1, the CME has moved out significantly and reached close to the edge of the coronagraphic field of view. Frame 2 also reveals more structures behind the leading edge of the CME. Notable are the compact
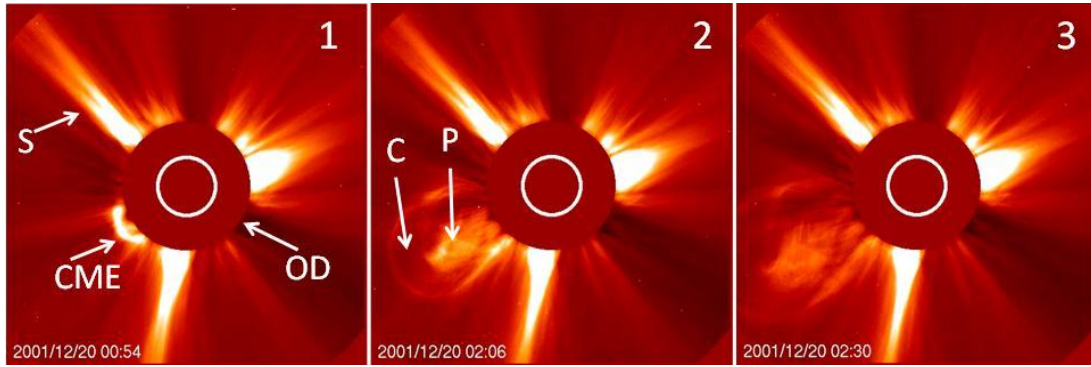
Figure 1. Illustration of a CME from SOHO/LASCO observed on 2001 December 20. Three frames of the coronagraphic observation are shown. The white circle represents the optical Sun. The solid disk is the image of the occulting disk. The cavity (C) and the prominence (P) are substructures of the CME.

bright feature marked "P" and the void region (marked "C") below the leading edge and roughly surrounding P. In frame 3, the CME leading edge has moved past the field of view of the coronagraph. Note that all the streamers remain roughly unchanged. Many of the streamers may also erupt eventually because these streamers overly closed field regions on the Sun, which are the source regions of CMEs. The feature C appears dark because it has less plasma density, but is likely to contain higher magnetic field (for pressure balance). In fact, the void structure contains helical field lines as inferred from observations made when the CME expands into the interplanetary (IP) medium and blows past spacecraft such as Wind and ACE. The central bright structure is the prominence material that erupts along with the CME and often referred to as the "core". The void region is also known as the cavity. Cavities can be seen in the pre-eruption stage in eclipse pictures.

Figure 2b shows another CME with the three-part structure as in the previous example: a structured bright core, void region and the bright front (FR) that identifies the flux rope (Chen et al.,1997). However, the streamer to the left of the CME shows a distortion that was not present in the image obtained earlier (Fig. 2a). The location of the distortion is marked "S" in Fig. 2b. When the pre-event image at 06:24 UT is subtracted from the 06:30 UT image, we see a diffuse structure that

surrounds the three-part structure (see Fig. 2c) and it precisely extends to the kink noted in Fig. 2b. In difference images, one observes only the bright feature surrounded by the diffuse feature. These structures are sometimes referred to as the main body and whole CME (Yashiro et al., 2008). The diffuse feature surrounding the flux rope is identified with the compressed plasma known as shock sheath (Gopalswamy, 2009; Gopalswamy et al., 2009d; Ontiveros and Vourlidas, 2009). The shock itself is too thin to be observed in coronagraphic images. The diffuse structure is only observed in relatively fast CMEs. Although there have been attempts to search for white-light features of the shocks in the past (Sheeley et al., 2000; Vourlidas et al., 2003), the diffuse feature has been recognized as a shock manifestation only recently (Gopalswamy, 2009; Gopalswamy et al., 2009d; Ontiveros and Vourlidas, 2009; Gopalswamy, 2010a). Thus, fast CMEs have an additional shock sheath structure and hence should be referred to as CMEs with a four-part structure. Superposed on the LASCO image is an EUV difference image that displays changes taking place in the low corona normally blocked by the occulting disk. The EUV image shows a large scale disturbance on the disk indicating that the CME originated on the visible disk. The CME had a speed of 2050 km/s, nearly five times the average speed of all CMEs (see section 2.4.1).
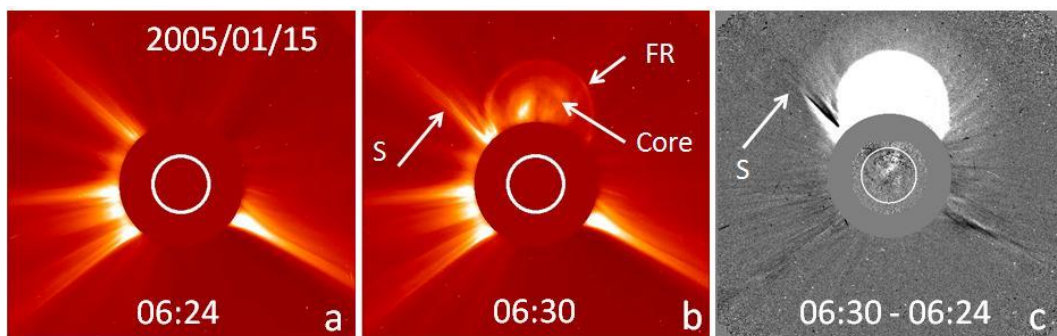

Figure. 2 Pre-event (a) and event (b) images of a fast CME and the difference between the two (c). In (c), an EUV difference image from SOHO's Extreme-ultraviolet Imaging Telescope (EIT) is superposed to see the activity on the disk in the CME source region (from Gopalswamy 2010a).

2.2 Solar Source of CMEs

CMEs occur from closed magnetic field regions, where magnetic free energy is stored and released during eruptions. A closed field region can be a simple bipole, an active region, or a quiescent filament region. In photospheric magnetograms, all these regions show positive and negative polarity patches and it is expected that field lines connect from the positive part to the negative part. There is a polarity inversion line, also known as the neutral line, where the line-of-sight field vanishes. A dark filament often overlies the neutral line and becomes part of the CME (prominence core) when the region erupts. Flares also occur in these regions in association with CMEs. Flares occurring without CMEs are known as confined flares because loops connecting the two polarities suddenly brighten with no significant mass motion away from the solar surface.

The closed magnetic field region is generally referred to as the solar source or source region of a CME. After a CME eruption, one can see in X-ray, EUV or microwave images a set of loops in the corona straddling the neutral line. This arcade is referred to as "post-flare loops", "arcade formation", "flare arcade", or "post-eruption arcade". The centroid of the arcade is often taken as the flare location. In H-alpha pictures, the feet of these loops are observed as two ribbons roughly parallel to the neutral line. The ribbons are the chromospheric manifestation of the eruption.

Figure 3 shows the source region of the 2006 Dec 14 CME at 22:30 UT observed by SOHO/LASCO. The CME was shock-driving as evidenced by the diffuse feature surrounding the bright CME in the south-east quadrant. The solar source is obtained by superposing a EUV difference image taken at 22:24 UT. The image taken at 22:12 UT was subtracted from the image taken at 22:24 UT to see the change taken place between the two frames. In the EUV difference image, one can see a compact flare on the disk surrounded by an EUV wave (Thompson and Myers, 2009 and references therein; Veronig, et al., 2008). The EUV wave is considered to be the "ground track" of the CME shock, the ground level being the inner corona seen in 195 Å. The magnetic structure of the source region (active region 10930) is revealed in the SOHO/MDI magnetogram taken just before the eruption. Two other EUV images of the active region are also shown, which reveal the location of the flare right at the center of the active
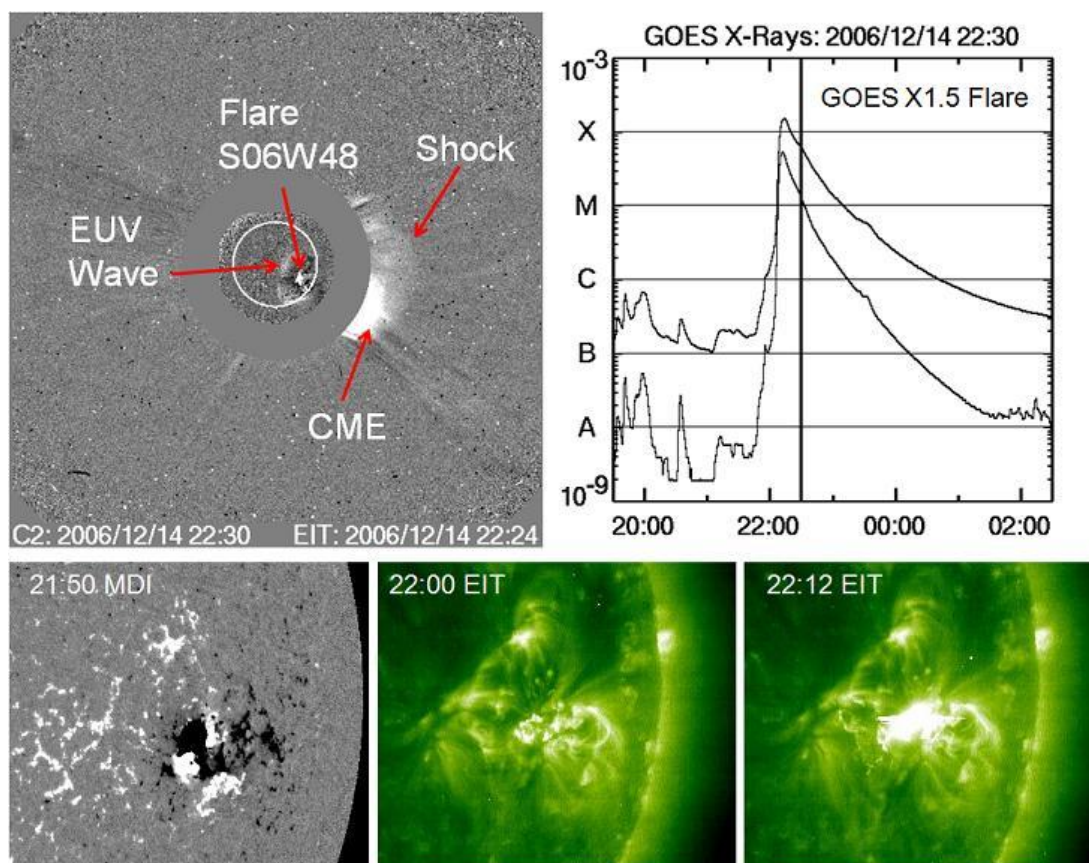

Figure 3. (top-left) The solar source of the 2006 December 14 CME, with the flare, EUV wave, and the shock surrounding the CME marked. (top-right) The GOES soft X-ray light curve showing the X1.5 flare. The vertical line marks the time of the CME in the top left panel. (bottom-left) Photospheric magnetogram taken just before (21:50 UT) the onset of the eruption showing active region 10930 as a complex region. The white and dark regions represent positive and negative magnetic polarities, respectively. (bottom-middle) SOHO/EIT image taken just before the eruption (22:00 UT). (bottom-right) The bright flare loops (not resolved) occurring at the center of the active region.
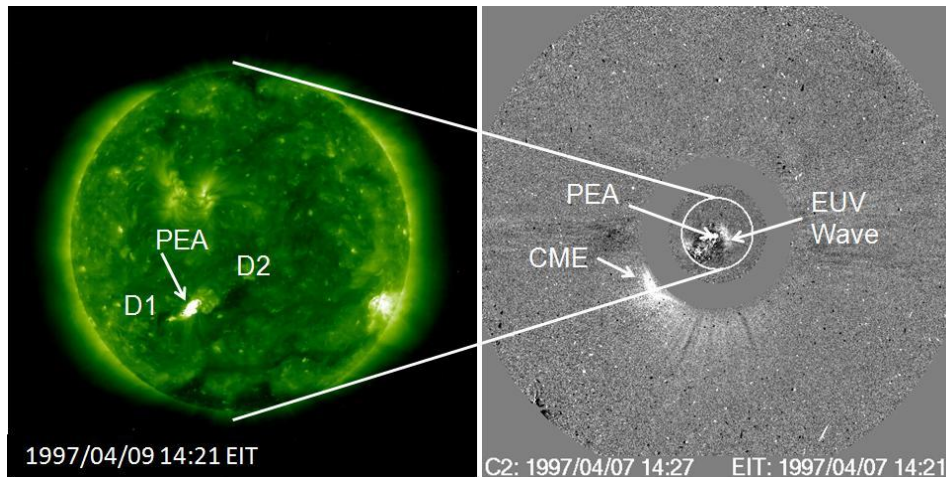
Figure 4. Another solar eruption observed by SOHO/EIT (left) and LASCO (right). The EUV image on the left shows the solar source as a post eruption arcade (PEA) and two dimming regions (D1, D2) on either side of the PEA. The LASCO difference image shows the CME appearing above the southeast limb of the Sun. The superposed EUV difference image at 14:27 UT shows a EUV wave roughly surrounding the PEA. The large-scale disturbance between the EUV wave front and the PEA is considered to be a manifestation of the CME.

region. Figure 3 also shows the soft X-ray flare light curve obtained by the Geostationary Operational Environmental Satellites (GOES) in two wavelength channels (1 – 8 Å upper curve and 0.5 – 4 Å lower curve). Flares in general can have intensity varying over several orders of magnitude, starting below A-class ($<1.0x10^{-8}$ Wm^{-2}) and beyond X-class ($>1.0x10^{-4}$ Wm^{-2}). The flare in question is of X-class (X1.5, which means the peak soft X-ray flux is $1.5x10^{-4}$ Wm^{-2}). One can also use X-ray, microwave and H-alpha pictures to identify the source region. Each represents a slightly different manifestation of the eruption. It is difficult to identify the solar sources of CMEs occurring behind the limb. If the sources are within a few tens of degrees behind the limb, one can still observe EUV disturbances above the limb with no signature on the disk.

Figure 4 shows another eruption from the southeast quadrant of the Sun. The eruption region shows the post-eruption arcade (PEA) surrounded by a large-scale disturbance in EUV, similar to the one shown in Fig. 3. The EUV wave is located at the outer edge of the large-scale disturbance. The EUV image to the left shows two dark regions on either side of the PEA. These are known as coronal dimming regions, thought to be the sites where the CME legs are rooted. The dimming represents an evacuation of coronal material as part of the eruption process. The coronal dimming and the large-scale disturbance have become important signatures of CME eruption, often useful in connecting CMEs to their IP consequences (Hudson and Webb, 1997; Gopalswamy, 1999; Hudson and Cliver, 2001).

2.3. Physical Properties

CMEs contain coronal material at a temperature of a few MK in the outer structure with cool prominence material (~8000 K) in the core. When the CME is shock-driving, the compressed sheath behind the shock can have higher temperature and density than in the ambient corona (see Fig. 2c). The density in the inner corona is typically 10^{8-9} cm^{-3} and is expected to be present in the frontal structure of CMEs close to the Sun. Density estimates from white light (see e.g., Vourlidas et al., 2002), radio (Gopalswamy and Kundu, 1992; 1993) and ultraviolet (Ciaravella et al., 2003) observations are consistent with such densities. Prominences are much denser (10^{10-11} cm^{-3}). The cavity is certainly of lower density compared to the frontal structure and prominence core. The magnetic field of the CMEs near the Sun is unknown. The field strength in prominences has been measured: ~3-30 G in quiescent prominences and 20-70 G in active prominences, occasionally exceeding 100 G (see, e.g., Kim and Alexeyeva, 1994). The magnetic field in the cavity is virtually unknown. However, one can infer from pressure balance arguments that the cavity must contain higher magnetic field strength because of its lower density. When the cavity rises as the CME flux rope, it may trap nonthermal electrons accelerated during the eruption, producing what are known as moving type IV radio bursts. These bursts have high degree of polarization (>70%), which requires a magnetic field strength of ~10 G near the Sun (~1.5 Rs) and ~2 G at a distance of ~4 Rs (Dulk and McLean, 1978). Bastian et al. (2001) obtained an order of magnitude lower field strength for a CME.

2.4. Statistical Properties

There have been many studies on the statistical properties of CMEs since their discovery (see, e.g., Hundhausen, 1993; Howard et al., 1985; Howard, 2006; Gopalswamy 2004; 2006a,b; Kahler, 2006; Gopalswamy et al., 2009a; 2010a). The following is a summary of CME properties based on SOHO/LASCO observations.

2.4.1 CME Speed

CMEs liftoff from rest, which means the speed changes with time very early on. The driving force of CMEs is expected to act close to the Sun (within a few Rs). Far into the solar wind, the driving force probably weakens, but the interaction with the ambient medium (drag force) tries to slow the CMEs. Once the solar wind picks up, the drag force may decrease slightly because the drag depends on the difference between the CME and solar wind speed. The CME speed is a basic attribute, defined as the average speed within the coronagraphic field of view (FOV) by fitting a straight line to the height – time measurements in the sky plane. The speed is close to the actual speeds only for CMEs propagating in the sky plane. CMEs ejected at an angle to the sky plane are subject to projection effects, so the measured speed is a lower limit. Figure 5 shows that the speed varies over two orders of magnitude from 20 km/s to more than 3000km/s, with an average value of 466 km/s. The average speed is virtually the same as the ones obtained from pre-SOHO observations.

2.4.2 Angular Width

The angular width is measured as the position angle extent of the CME in the sky plane, so only those CMEs that are in the sky plane (solar source near the limb) will yield the true width. Figure 5 shows that the apparent width (W) ranges from <5° to 360° with an average value of 41°. To compute the average, we used CMEs with widths <120° because the higher values generally are due to projection effects. Note that the last bin (W = 360°) has a higher value than most other bins in the range 120° – 360°. The CMEs in the 360° bin are known as halo CMEs (Howard et al. 1982). Halo CMEs appear to surround the occulting disk in the sky plane projection. In reality, these are like any other CME, except that they expand rapidly beyond the extent of the occulting disk. Halo CMEs constitute only ~3% of all CMEs. Halo CMEs and the ones with 120° ≤ W< 360°

constitute an important subset because they are very energetic and hence have significant effect on the heliosphere. Halo CMEs are discussed in section 3.

2.4.3 Acceleration

The linear fit (constant speed) to the height – time measurements is a good approximation only for some CMEs and a second order (constant acceleration) fit is better for others. The derived acceleration generally depends on the initial speed (or its square) within the coronagraphic field of view (Gopalswamy et al., 2001a; Yashiro et al., 2004). Of course the acceleration is not constant because of the different radial variations of the propelling and retarding (gravity, drag) forces acting on the CME (see e.g., Vršnak et al., 2004). Within the coronagraphic FOV, CMEs moving faster than the slow solar wind decelerate, while the slower ones accelerate. CMEs with speeds close to that of the slow solar wind move with a constant speed. A scatter plot between the observed acceleration (*a*) and the CME linear speed (*V*) shows a weak correlation with the regression line (Gopalswamy, 2006b):

$$a = -0.015 \, (V - 466). \quad \ldots\ldots\ldots\ldots\ldots\ldots\ldots(1)$$

One can associate the 466 km/s as the typical slow solar wind speed (see Gopalswamy et al., 2000). This equation is only approximate because the CME propulsion and gravity may still be playing a role in the coronagraphic FOV.

Figure 6. shows that the average CME acceleration within the LASCO FOV is close to zero with an average value of 0.7 ms^{-2}. To avoid projection effects, we considered limb CMEs (solar sources within 30° from the limb) associated with flares of size ≥ C3.0. With these restrictions, the average value shifts to - 3.1 ms^{-2}. The C3.0 restriction eliminates a lot of slow and narrow CMEs with questionable flare association, which mostly contribute to the positive acceleration, consistent with equation (1).
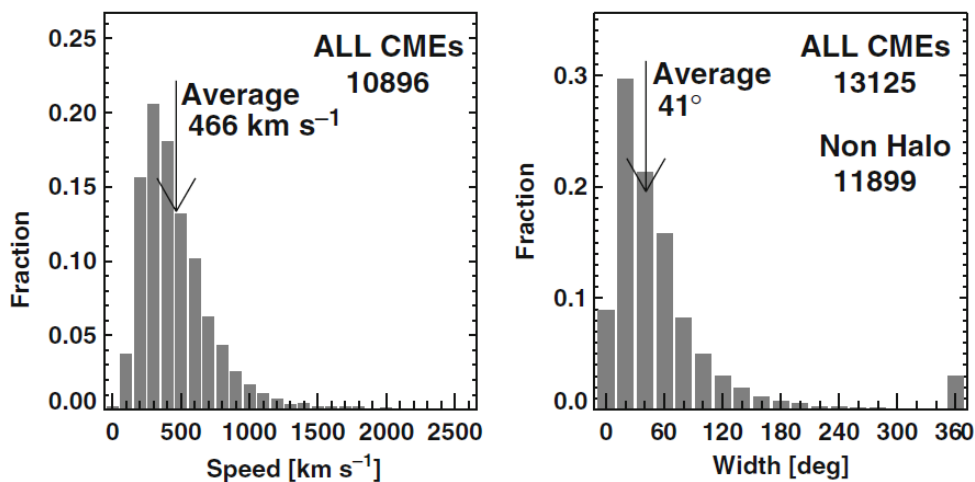

Figure 5. Speed and width distributions of SOHO/LASCO CMEs (1996 – 2007). For computing width distribution, only CMEs with width <120° are considered.
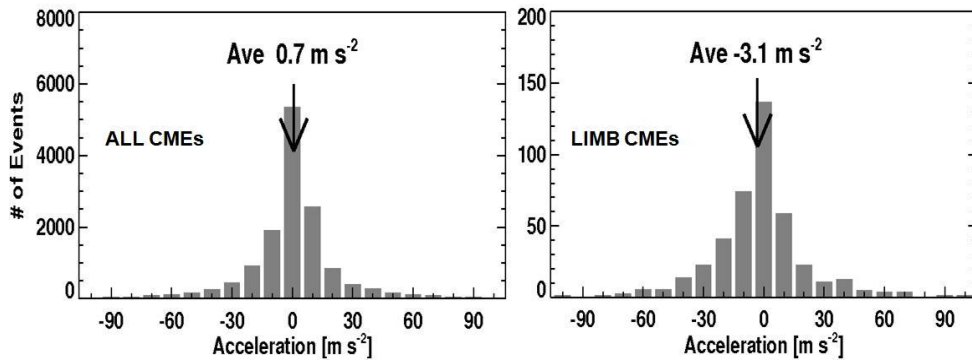
Figure 6. Distributions of CME acceleration obtained from a quadratic fit to the height – time measurements for all CMEs (left) and limb CMEs (right). The period considered: 1996 – 2009.
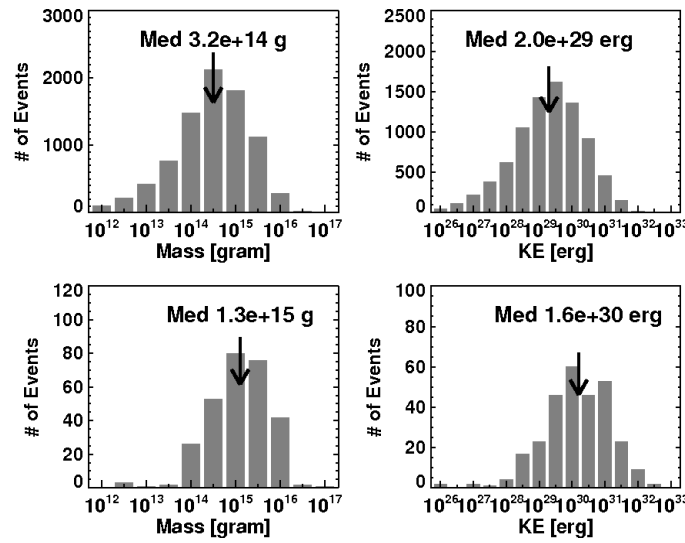

Figure 7. Mass and kinetic energy distributions of SOHO/LASCO CMEs (1996 – July 2008). The median values of the distributions are marked on the plots.

2.4.4 Mass and Kinetic Energy

The CME mass (computed as the excess mass in the coronagraphic FOV) ranges from $<10^{12}$ to $>10^{16}$ g with a median value of $\sim3.2\times10^{14}$ g (see Fig. 7). The CME mass is computed by estimating the number of electrons needed in the sky plane to produce the observed CME brightness. Wider CMEs generally have a greater mass content (Gopalswamy et al. 2005a):

$$\log M = 12.6 + 1.3 \log \dots\dots\dots\dots\dots\dots\dots \text{(2)}$$

where M is the mass in grams and W is the width in degrees. The CME speed (V in km/s) is also related to its width (Gopalswamy et al., 2009b):

$$V = 360 + 3.64\, W, \dots\dots\dots\dots\dots\dots\dots\dots \text{(3)}$$

indicating that wider CMEs are generally faster and more massive because of equation (2). Thus faster and wider CMEs have a higher kinetic energy. Using the speed and mass measurements, one can compute the CME kinetic energy (see Vourlidas et al., 2010 for more details). The kinetic energy ranges from $<10^{26}$ to $>10^{33}$ erg, with a median value of 2.0×10^{29} erg. If we limit

ourselves to limb CMEs, as we did when estimating the CME acceleration, the distributions of mass and kinetic energies become more symmetric and the median values become several times greater: 1.3×10^{15} g and 1.6×10^{29} erg, respectively. The higher values are consistent with pre-SOHO values (see e.g., Howard et al., 1985) because those coronagraphs were not sensitive enough to detect fainter CMEs.

2.4.5 CMEs and Flares

The CME and flare in a given eruptive event are thought to be two different manifestations of the same energy release (see e.g., Harrison 1995). Case studies in the past have also indicated tight relationships between flares and CMEs, whenever a flare is associated with a CME (Zhang et al., 2001; Vršnak et al., 2004). As we noted in Fig. 3, CMEs are always accompanied by solar flares, especially if we use soft X-ray enhancement to identify flares. However, the opposite is not true: not all flares are associated with CMEs. Figure 8 describes some known relationships between CMEs and flares. The CME association rate steadily increases with flare
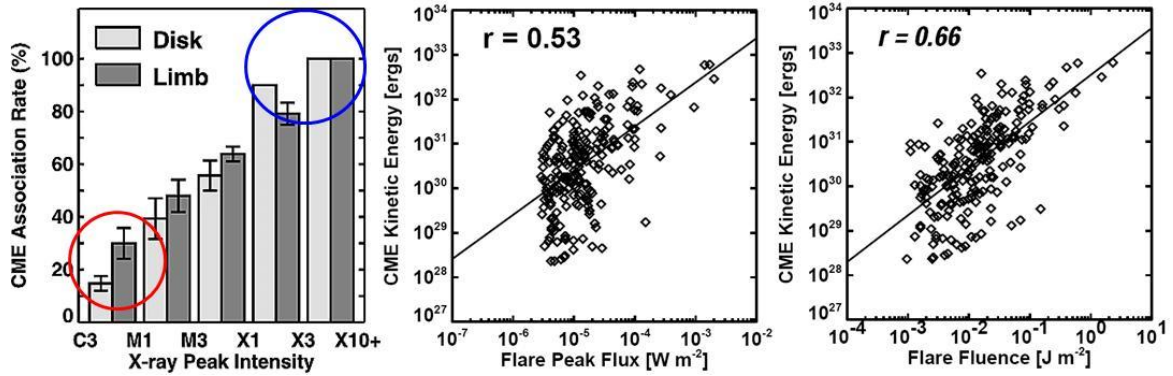
Figure 8. (left) CME association rate of flares (≥ C3.0) from the disk and limb (from Yashiro et al., 2004). (middle) Scatter plot between soft X-ray flare size and CME kinetic energy. (right) Scatter plot between flare fluence and CME kinetic energy (from Gopalswamy, 2010a).
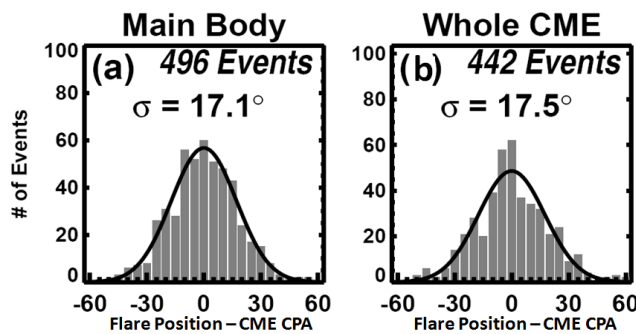

Figure 9. Distributions of the offset of flare positions with respect to the central position angle (CPA) of the associated CMEs (from Yashiro et al., 2008).

size from 20-30% for C-class flares to 100% for X-class flares with intensity >X3.0 (Yashiro et al., 2005). Limb and disk flares are separated to avoid the CME visibility issue. We see that there are a large number of flares without CME association. There are even X-class flares that are not associated with CMEs. Such flares are known to be confined flares with no accompanying mass motion (Gopalswamy et al., 2009c).

For flares with CMEs, there is a reasonable correlation between flare size in soft X-rays and the CME kinetic energy (Hundhausen, 1999; Moon et al., 2002; Gopalswamy et al., 2009b; Yashiro and Gopalswamy, 2009). Figure 8 shows that the correlation coefficient between the CME kinetic energy and the peak soft X-ray flux is only 0.53 (0.66 when soft X-ray fluence is used) suggesting that the partition between heating and mass motion may not be uniform in all eruptions. Limb events were chosen for the scatter plots to avoid projection effects in the measured speeds and masses to get the kinetic energy. Another interesting relation between CME width and the angular extent of the flare arcade was obtained by Moore et al. (2007). They showed that final width of the CME can be estimated from the amount of magnetic flux covered by associated flare arcade.

The eruptions showed in Figs. 3 and 4 show an important spatial property of the flare – CME connection. The CMEs are located radially above the flare arcade in both cases. The diffuse disturbance surrounding the CME is also located radially above the

arcade, but with less precision. In the pre-SOHO era results from studies using small samples (~10 CMEs) indicated that the flare is located anywhere under the span of the CME (Harrison, 2006; Kahler et al. 1989). A recent statistical study using nearly ~500 CMEs showed that most of the leading edges of CMEs are positioned directly above the flare site (Yashiro et al., 2008). Figure 9 shows the statistical result for both CMEs (main body) and the surrounding disturbances (whole CME). The standard deviation is only ~17°, which is roughly the angular extent of the flare structure (PEA in Figs. 3 and 4, see also Gopalswamy, 2008a).

2.4.6 CME Occurrence Rate

How frequently do CMEs occur is an important question from a practical point of view and may act as a solar activity index. Figure 10 shows that the daily CME rate averaged over Carrington rotation periods ranges from <0.5 (solar minimum) to > 6 (solar maximum). These are only average values, but individual days are known to have more than 10 CMEs per day (Gopalswamy et al., 2003a). The daily rate shown in Fig. 10 is much higher than the rates obtained by pre-SOHO coronagraphs (see e.g., Cliver et al. 1994) probably because SOHO/LASCO has better dynamic range and wider FOV so it can observe fainter CMEs. The flare occurrence rate is much larger than that of CMEs because not all flares are associated with CMEs as discussed before. The overall time development of
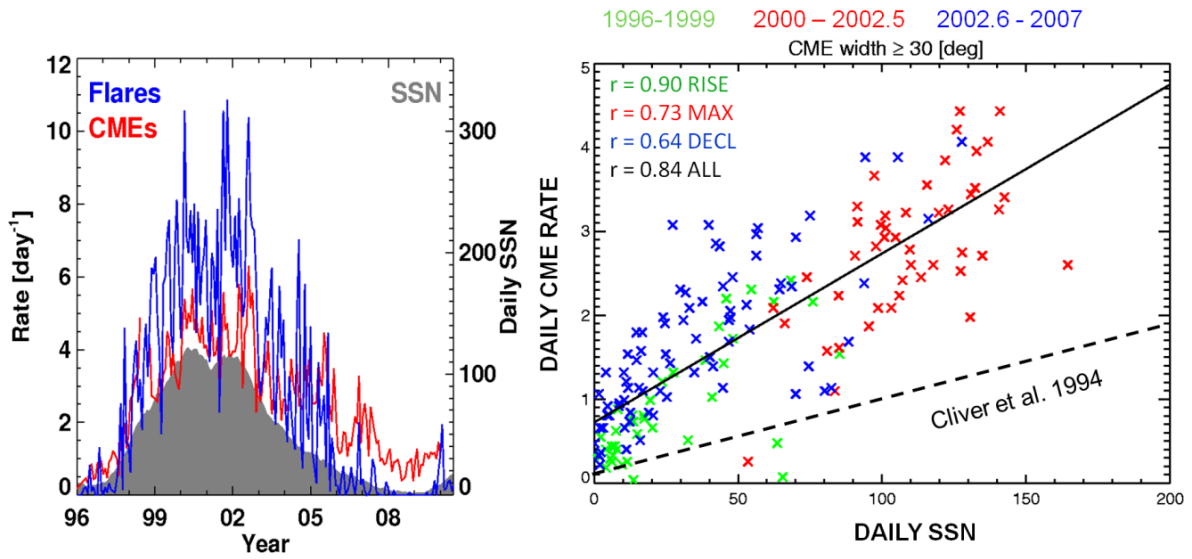
Figure 10. (left) Daily CME and soft X-ray flare rates compared with daily sunspot number (SSN). CMEs under the category "Poor" have been excluded. For flares, C-class and above are used. (right) Scatter plot of CME daily rate as a function of SSN. The three phases of the solar cycle are distinguished. The regression line for all the data is shown (CME Rate = 0.02SSN + 0.7). For comparison, the pre-SOHO regression line (CME Rate = 0.011SSN + 0.06) is shown from Cliver et al. (1994) (dashed line). CMEs with width > 30° were used in the plot (adapted from Gopalswamy et al 2010a).

the CME and flare rates follows that of the sunspot number (SSN). The scatter plot between Daily SSN and the CME rate also shows the solar cycle variation of the CME rate (see Fig. 10 right). The CME rate and SSN in Fig. 10 shows a good correlation with the regression line (Gopalswamy et al., 2010a):

CME rate = 0.02SSN + 0.7, ………………….. (4)

with a correlation coefficient r =0.84. The regression line is quite different from the one obtained from pre-SOHO observations (Cliver et al., 1994):

CME Rate = 0.011SSN + 0.06. ……..…………. (5)

Note that both the slope and the intercept in equation (5) are lower than the corresponding values in equation (4).

This means the pre-SOHO observations underestimated both the CME rate and the residual rate that corresponds to CMEs from non-sunspot sources. The high correlation between SOHO CME rate and SSN given in equation (4) is not uniform throughout the solar cycle. The correlation is high during the rise (r = 0.90) and declining (r = 0.73) phases, but is lower during the maximum phase (r = 0.64). The low correlation has been attributed to CMEs originating from non-spot regions, e.g., from polar crown filament regions, which occur exclusively outside the sunspot zone. Figure 11 illustrates the abundance of high-latitude eruptions using prominence eruptions (PEs) observed by the Nobeyama radioheliograph and the associated CMEs observed by SOHO/LASCO: there are many eruptions
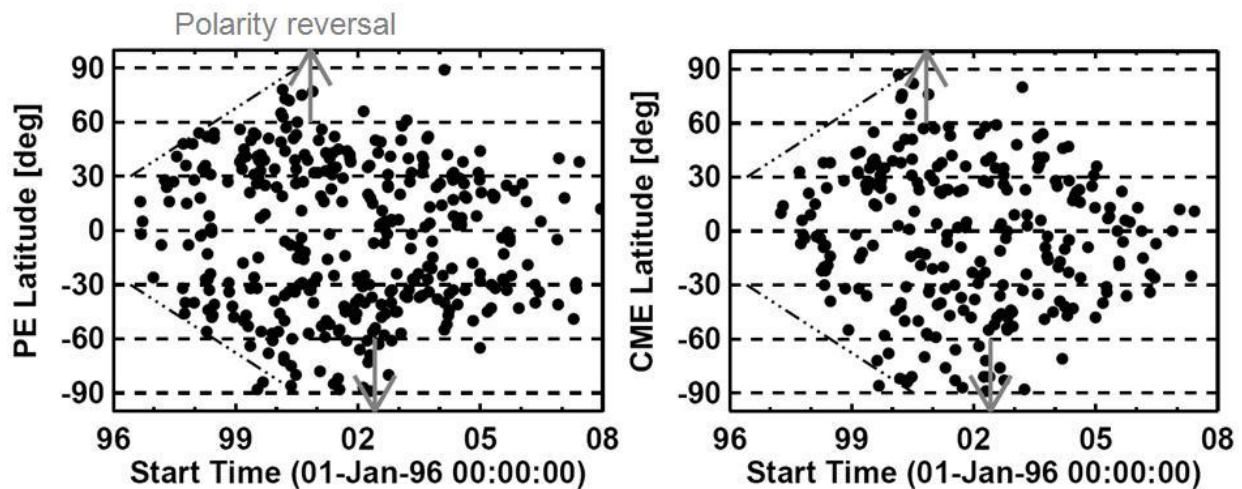

Figure 11. The latitude distribution of prominence eruptions (left) and the associated CMEs (right). The up and down arrows represent the times of polarity reversal at the north and south poles, respectively (updated from Gopalswamy et al., 2003a).
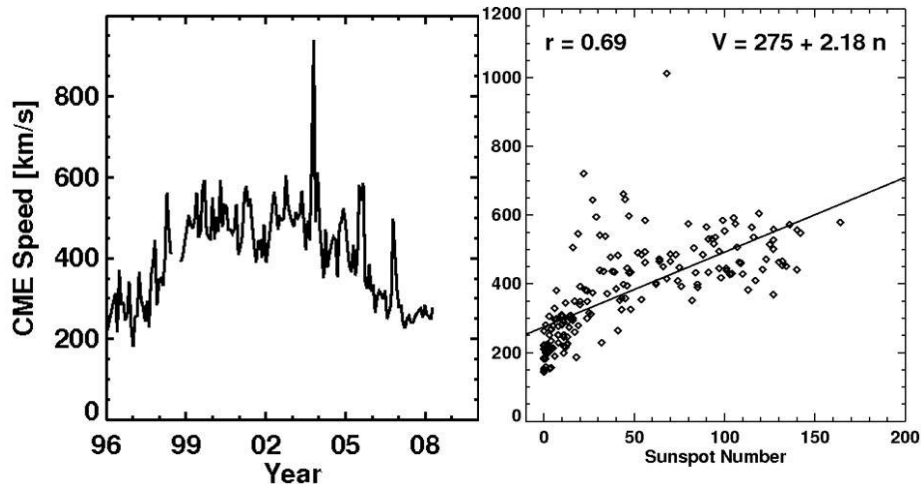
115

Figure 12. (left) Variation of CME speed as a function of time. The plotted speed is computed as an average of all CMEs occurring in a Carrington rotation period. The large spikes are due to super-active regions that produced many CMEs in quick succession. (right) The scatter plot between the average CME speed as a function of the sunspot number. The regression line and the correlation coefficient are shown.

at latitudes $\geq 60^{\circ}$ over a three year period between the middle of 1999 and the middle of 2002. There is also a north-south asymmetry in the number and the occurrence epoch of high-latitude CMEs. The end of the high-latitude activity coincides with the polarity reversal at each pole (Gopalswamy et al., 2003b). Sunspots originate at latitudes below $\sim 40^{\circ}$, so the CMEs originating at $\geq 60^{\circ}$ latitudes have no relation to sunspots and hence contribute to the low correlation between the CME rate and SSN.

2.4.7 Solar Cycle Variation of CME Speeds

CMEs derive their energy from the magnetic fields in solar active regions, which contain intense magnetic fields during the solar activity maximum. Therefore, one expects more energy going into the CMEs during the maximum phase. Pre-SOHO observations were contradictory in the solar cycle variation of the CME speed (see Gopalswamy et al., 2003a for a discussion on the CME speeds from observations by SMM and P78-1 satellites). SOHO observations clearly showed the solar cycle variation of CME speeds beyond any doubt (Gopalswamy et al., 2003a; Gopalswamy, 2006b). Figure 12 shows the mean speed of CMEs averaged over Carrington rotation periods. The speeds are smaller because of the averaging process. Recall that individual CMEs can have speeds exceeding 3000 km/s. The spikes in the speed curve are due to CMEs from some super active regions that produced energetic CMEs in quick succession (Gopalswamy et al., 2006). The largest spike is due to CMEs from the 2003 Halloween events (Gopalswamy et al., 2005b). One can see an overall increase in the CME speed by a factor of $2 - 3$ between the minimum and maximum periods. The speed dip between the years 2001 and 2002 is similar to the CME and flare occurrence rates (Gopalswamy, 2004).

Figure 12 also shows a scatter plot between the average speed and the sunspot number. The correlation

is relatively high (r = 0.69), although smaller than the CME rate – SSN correlation. Data points showing major deviation from the regression line (V = 275 + 2.18SSN) are due to the super active regions corresponding to the spikes in the time variation plot in Fig. 12. When the spikes are excluded, the correlation becomes much better.

3. Halo CMEs

As we noted in section 2.4.3, halo CMEs are so called because they appear to surround the occulting disk of the coronagraph and were first identified by the Solwind coronagraph on board the P78 – 1 satellite in an image taken on 1979 November 27 (Howard et al., 1982). The 3-D nature of CMEs became immediately evident from this observation: the CME appeared as a cone projected on the sky plane. This is illustrated in Fig. 13 where the three cones 1, 2, and 3 represent three CMEs heading from the Sun toward the observer. The region between the two parallel lines is blocked by the occulting disk. CME 1 expands very fast and shows up outside the occulting disk and hence appears to surround the occulting when it is very close to the Sun. CME 2 has to move a longer distance before appearing above the occulting disk. CME 3 has to move still farther to be seen as a halo. In principle, even a narrow and slow CME can become a halo if the coronagraph has infinite sensitivity. Fig. 14 illustrates that halo CMEs are normal CMEs using the two views of the STEREO mission.

In the STEREO Ahead (SA) view, the solar source is closer to the east limb so the CME appears as a regular CME (Fig. 14 right). In the STEREO Behind (SB) view, the solar source is near the disk center (directly facing the spacecraft), so the CME appears as a halo (Fig. 14 left). In the SB view, what is observed is just the outermost disturbance (marked by dashed arrows). On the other hand, both the main body of the CME (marked by solid arrows) and the outermost disturbance are
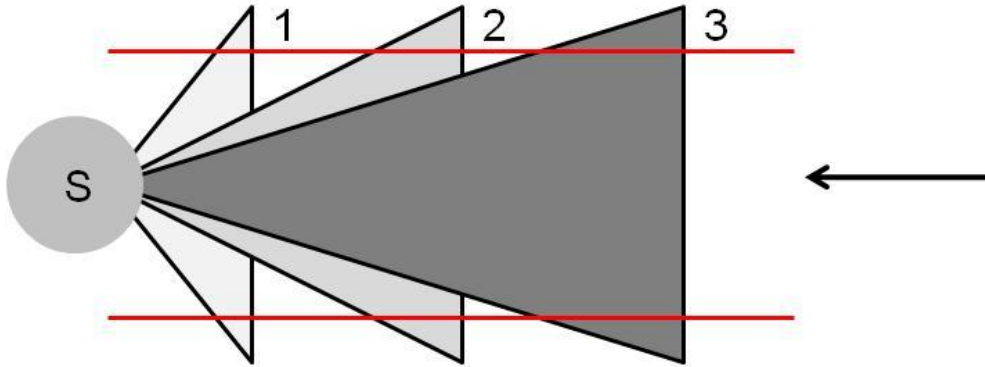
Figure 13.Three cones marked 1, 2, and 3 with their apex at the Sun and base toward the observer and represent three halo CMEs. The two horizontal lines mark the inner edge of the coronagraph FOV because of the occulting disk. Note that only the CME portions outside the two horizontal lines will be seen projected against the sky plane. In the view perpendicular to the paper, the CMEs appear as normal CMEs (adapted from Gopalswamy et al., 2009g).
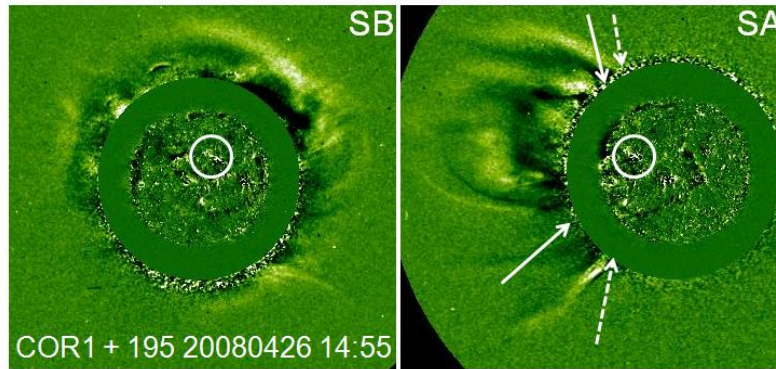

Figure 14. The 2008 April 26 CME imaged simultaneously by STEREO Ahead (SA, right) and STEREO Behind (SB, left). The spacecraft were separated by ~50°. The CME is a halo in the SB view, but a normal CME in the SA view. The solid (dashed) arrows point to the CME (disturbance) angular extent. The solar source of the CME is shown encircled in the difference image taken by STEREO's Extreme Ultraviolet Imager (EUVI). The elongated feature is the post eruption arcade. The halo CME is roughly symmetric around the solar source, while the CME is mostly to the east from Earth.

observed in the SA view. Thus, a top view produces a halo CME, while a broadside view produces a normal CME. Occasionally, the two dashed arrows can come close to each other, in which case the CME becomes a halo even in the broadside view; such CMEs are known as "limb halos" because the disturbances can be seen on the limb opposite to the solar source. Such limb halos

are generally the fastest events (average speed ~ 2000 km/s). Recall from equation (3) that the CME width and speed are correlated, so wider CMEs are generally faster and hence become halos early on.

Figure 15 shows the speed distribution of all halos observed by SOHO/LASCO during cycle 23. Also shown is the histogram of flare sizes associated with the
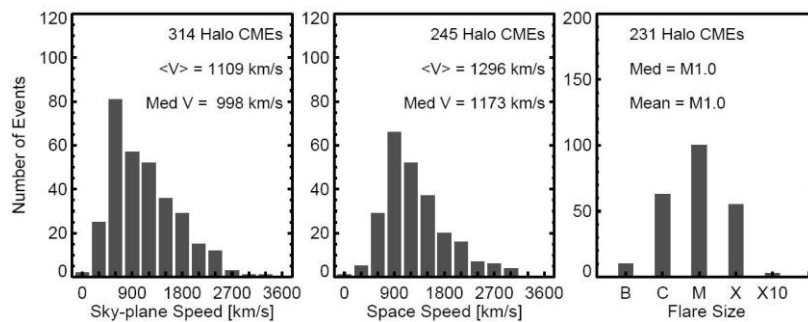

Fig. 15. Distributions of speeds (sky-plane and space) and flare size of halo CMEs. The average and median values of the distributions are shown on the plots (adapted from Gopalswamy et al., 2009g).

117

halo CMEs. Clearly, the average speed of halo CMEs (corrected for the projection effects or not) is more than double the average speed of the general population. Similarly, the average flare size is M1.0, an order or magnitude large than for the general population (see Gopalswamy et al., 2007). Thus halo CMEs represent a population of higher-than-average energy, which is useful in assessing the average energy of various CME populations: higher the fraction of full halos, larger is the average energy. Halo CMEs have practical consequences, since they are likely to arrive at the observing spacecraft in a couple of days, depending on the speed.

4. CMEs and Shocks

There are many signatures of CME-driven shocks. Type II radio bursts represent the earliest signature of CME-driven shocks. Type II bursts are known for more than sixty years, since their first recognition in radio light curves obtained by Payne-Scott et al. (1947), who immediately recognized that the bursts must be related to mass ejection from the Sun. It was soon recognized that fast mode MHD shocks must be responsible for the type II bursts (Uchida, 1960). One-to-one correspondence between type II bursts at much longer wavelengths and CMEs were found in the 1980s (Cane et al., 1987). Finally, all the type II bursts in the intermediate (decameter – hectometric or DH) wavelengths were also found to be associated with CMEs (Gopalswamy et al., 2001a). The CME leading edge can be as low as at 1.3 Rs when the type II burst starts at metric wavelengths (Gopalswamy et al., 2005a; 2009d).

Sudden commencement of geomagnetic storms (SSC) is another signature of IP shocks recognized in the magnetometer data. Interplanetary shocks were proposed to be responsible for SSCs in 1953 (Gold, 1955), which was soon confirmed by Mariner 2 observations (Sonett et al., 1964). An energetic storm particle (ESP) event, starting at the time of the shock arrives at an observing spacecraft, is another signature of IP shocks (Bryant et al., 1962). Similarly, shocks are inferred from solar energetic particle (SEP) events, which start soon after the ejection of energetic CMEs from the Sun (Reames, 1999). Although SEP events are known for several decades, it was Kahler et al. (1978) who recognized the importance of CMEs for the occurrence of SEP events. CME-driven shocks are routinely detected in the solar wind using plasma and magnetic field signatures as discussed below. Sheeley et al. (1985) made a clear connection between the CMEs observed near the Sun and the shocks observed in the IP medium. We already discussed the white light signatures of CMEs in the section 2.1. In this subsection, we concentrate on radio signatures of CMEs.

The radio signature of shocks arises as follows: the CME drives the shock. The shock accelerates nonthermal electrons, which in turn produce Langmuir waves in the vicinity of the shock. The Langmuir waves are converted into electromagnetic radiation (type II burst) at the fundamental and harmonic of the local plasma frequency. As the shock moves away from the Sun, the emission occurs at progressively lower frequencies. Since the emission frequency is proportional to the square root of the local plasma density, one can get information on the ambient density. The frequency drift rate gives information on the shock speed. Type II bursts occur at frequencies below ~150 MHz, although occasionally they are observed at higher frequencies (e.g., Vršnak et al., 1995). The cutoff at 150 MHz occurs at a heliocentric distance of ~1.5 Rs, which corresponds to the outer layers of active regions. At distances <1.5 Rs, one encounters high magnetic field of the active region and hence high Alfven speed not conducive for shock formation (Gopalswamy et al., 2001b). Type II bursts at frequencies above the ionospheric cutoff (20 MHz) can be observed using ground based radio telescopes. To observe the type II bursts at longer wavelengths, one has to go to space. The gap that existed between kilometric (km) and metric (m) wavelengths was filled by the Radio and Plasma Wave Experiment (WAVES) on board the Wind spacecraft. The gap corresponds to decameter-hectometric (DH) wavelengths. Type II bursts occur at various wavelength ranges, schematically shown in Fig. 16.

While there is no doubt about the association between CMEs and type II bursts at DH and longer wavelengths, the association between CMEs and metric type II bursts has been controversial. The question is what drives the shocks: flare blast or CMEs. The blast wave scenario was supported by the observation of CMEless metric type II bursts (Sheeley et al., 1984). However, the sources of CMEless type II bursts were generally located close to the disk center (Cliver et al., 1999; Gopalswamy et al., 2001c). Coronagraphs are not well suited for observing CMEs originating close to the disk center (because of the coronagraphic occulting disk), especially the faint ones. Furthermore, with the advent of the EUV imagers, it is possible to detect large-scale disturbances surrounding the flaring region, which are the EUV manifestations of the CME (see Figs. 3 and 4). With SOHO observations, there seems to be no CMEless type II bursts. Even the handful of type II bursts claimed to be due to flare blast waves (Magdalenić et al., 2010) have CME association (although the CME speed ≤ 500 km/s). When only limb type II bursts are considered, there is 100% association with CMEs. Furthermore, all type II bursts occurring at DH wavelengths are associated with fast and wide CMEs (Gopalswamy et al., 2001a). These bursts typically originate at heliocentric distances >2 Rs. Combining these results with the past observations indicating that type II bursts at frequencies <2 MHz (Cane et al., 1987) are associated with fast CMEs, one can conclude that all type II bursts are associated with CMEs. This has been recently confirmed with a systematic study of type II bursts occurring at metric,
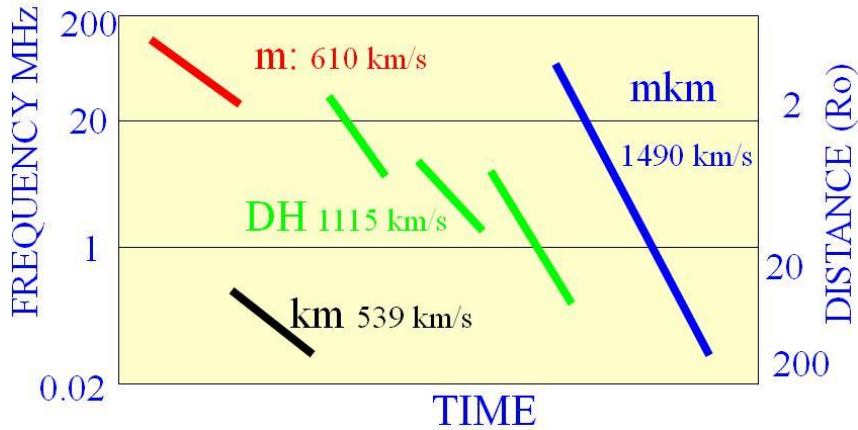
Figure. 16 Schematic dynamic spectrum showing variants of type II radio bursts occurring in the Sun-Earth connected space. Purely metric type II bursts (m) occur when the CME is within 2 Rs from the Sun center. The decameter – hectometric (DH) type II bursts have three variants as shown. Bursts starting at metric wavelengths and extending to kilometric (km) wavelengths are referred to as mkm type II bursts. The km type II bursts are those occurring at frequencies below 1 MHz. Sometimes type II busts start only in the kilometric wavelength range. The average CME speed corresponding to each type II variant is noted on near the bursts (adapted from Gopalswamy, 2006c).

DH, mkm and km wavelengths (see Fig. 16).

The CME kinetic energy (speed and width) organizes the type II populations : the average speed and halo fraction increase progressively as one goes from m to mkm type II bursts implying a progressive increase in kinetic energy (see Table 1). The most energetic CMEs obviously can drive shocks far into the IP medium, so the shock produces radio emission at various distances from the Sun (and hence at various wavelengths). Table 1 shows that in order to produce any variant of the type II bursts, the CME has to be faster than the average CME. Even the metric type II bursts need CME speed to be ~25% higher than the average speed of the general population. The purely km type II bursts have a lower CME speed than the m type II bursts do. This is because the associated CMEs continue to accelerate within the coronagraphic field of view, becoming super-Alfvenic only beyond ~10 Rs. This organization of type II bursts by CME kinetic energy lends support to the idea that the whole type II phenomenon can be explained by CME-driven shocks (Gopalswamy et al., 2005a).

Another argument in support of different sources for coronal and IP type II bursts has been the discordant drift rates for metric and IP type II bursts for a given CME event. This may be explained by the fact that the metric type II bursts are predominantly produced at the flanks of the CME-driven shock, while the IP type II bursts may be produced at the nose of the shock. Two

more things contribute to the discordance between the metric and IP type II bursts: (i) The Alfven speed profile changes drastically between the metric (< 2 Rs) and near-Sun IP medium (>2 Rs). (ii) The CME speed also changes rapidly in the metric domain, becoming constant or slowly declining in the two domains. Various combinations of these two effects can result in different behavior of metric and IP type II bursts (see Gopalswamy et al., 2001c; 2008a; Aguilar-Rodriguez et al., 2005).

4.1 Radio-Quiet CMEs

The clean dependence between CME energy and the wavelength range of type II bursts derived from Table 1 has some strong exceptions. There are many CMEs with speeds > 1000 km/s that have no type II burst association in any wavelength range. A compilation of fast (speed ≥ 900 km/s) and wide (width ≥ 60°) CMEs revealed that a large fraction of these energetic CMEs are radio quiet (Gopalswamy et al, 2008b). The radio quietness of CMEs is indicated by: (1) smaller speed and width (and hence lower kinetic energy) within the fast and wide population, (2) smaller soft X-ray flare sizes, and (3) eruption at large angles from the Sun – observer line. On the other hand, there are many radio-loud CMEs with speeds << 900 km/s in stark contrast to the radio-quiet fast and wide CMEs. This discrepancy can be explained by the role played by the ambient

Table 1. Properties of CMEs associated with different varieties of type II bursts. "All" denotes the general population of CMEs observed by SOHO from 1996 to the end of 2004 (Gopalswamy, 2006c).

Property	All	m	DH	mkm	km
Speed (km/s)	487	610	1115	1490	539
Width (deg)	45	96	139	171	80
Halos (%)	3.3	3.8	45.2	71.4	17.2
Acceleration (m/s^2)	−2	−3	−7	−11	+3

medium in deciding the shock-driving capability of CMEs. The characteristic speed (Alfven speed or fast mode speed) in the corona and interplanetary medium seems to vary over a factor of ~4 and can attain a value as high as 1600 km/s. Thus a 500 km/s CME can be radio loud while a 1600 km/s CME can be radio quiet depending on the characteristic speed of the medium through which the CMEs propagate. Some of these fast and wide CMEs may be shock driving, but the Mach number may be small rendering the shocks subcritical. Subcritical shocks are not efficient in accelerating particles in high numbers needed to produce the type II burst.

4.2 Radio-Quiet Shocks

The radio-quiet CMEs discussed above are fast and wide, but we do not know whether they drive shocks or not. If we start from CME-driven shocks observed at 1 AU, we are sure that the CMEs drive shocks. What are the radio-emission characteristics of these shocks? A surprisingly large fraction (~34%) of the 222 IP shocks observed during 1996 – 2006 was radio quiet (i.e., lacked type II radio bursts). CMEs associated with the radio-quiet shocks were generally slow (average speed ~535 km s^{-1}) and only ~40% of the CMEs were halos. The corresponding numbers for CMEs associated with radio-loud shocks were 1237 km s^{-1} and 72%, respectively. Thus, the CME kinetic energy seems to be the deciding factor in the radio-emission properties of shocks. The peak soft X-ray flux associated with the radio-quiet shocks was also low (C3.4 versus M4.7 for radio-loud shocks). CMEs associated with the radio-quiet shocks were generally accelerating (average acceleration ~+6.8 m s^{-2}), while those associated with the radio-loud shocks were decelerating (average acceleration ~ - 3.5 m s^{-2}). This suggests that many of the radio-quiet shocks formed at large distances from the Sun, typically beyond 10 Rs. The kinematics of the CMEs associated with the km type II bursts is similar to those of radio-quiet shocks, except that the former are slightly more energetic. Comparison of the shock Mach numbers at 1 AU shows that the radio-quiet shocks are

mostly subcritical, suggesting that they were not efficient in accelerating electrons. The 1-AU speeds of radio-quiet and radio-loud shocks were not too different even though they have completely different kinematics in the corona. This confirms that the interaction with the solar wind erases the difference between the two types of shocks.

5 CMEs in the IP Medium

CMEs travel far into the interplanetary medium, sometimes all the way to the edge of the solar system. Spacecraft in the solar wind routinely detect CMEs in the IP medium, referred to as IP CMEs or ICMEs. It must be noted that the idea of ICMEs and shocks precedes the discovery of white-light CMEs: the picture of a magnetic bottle driving a shock proposed by Gold (1962) is now the standard picture of ICMEs, except that the magnetic bottle is replaced by a flux rope. Koomen et al. (1974) recognized the similarity between the Gold magnetic bottle and CMEs observed by OSO-7 coronagraph. Burlaga et al. (1981) reported a complete ICME structure with shock, sheath, and the driving magnetic cloud using observations made by five spacecraft. Sheeley et al. (1985) found a close connection between CMEs observed near the Sun and IP shocks observed in the solar wind. Figure 17 shows the striking similarity between Gold's cartoon and a real SOHO/LASCO image.

Various plasma (temperature, plasma beta, flow speed, elemental and charge state abundances), magnetic field (field strength, field rotation), and particle (thermal and nonthermal) flux signatures are used to identify ICMEs (see Gosling, 1990; Neugebauer and Goldstein, 1997 for a review). Arrival of shocks at the spacecraft is also a good indicator of the impending ICME arrival except when the associated CME propagates at a large angle to the Sun-spacecraft line. Space observations made by a large number of spacecraft over the past several decades have shown that ICMEs can be found throughout the heliosphere (see e.g., Wang et al., 2005). In addition to the type II radio bursts discussed above, other techniques such as IP
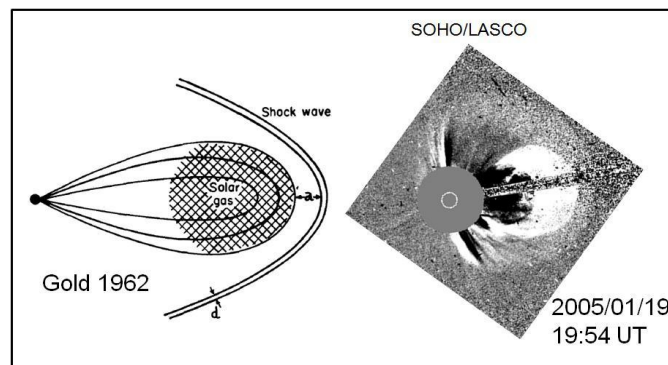

Figure 17. The Gold model of shock-driving magnetic structure compared with a SOHO/LASCO image. The bright feature in the LASCO image corresponds to the shock-driving magnetic structure. The diffuse structure surrounding the bright feature is the shock sheath. In the Gold (1962) cartoon, the standoff distance (a) and the shock thickness (d) are indicated.

scintillation observations (see e.g., Tokumaru et al.,2007) provide information on CME-driven shocks in the heliosphere.

ICMEs generally fall into two categories: flux ropes (field rotation) and non-flux ropes (also known as ejecta). Magnetic clouds (MCs) are a special subset of ICMEs that satisfy the following criteria (Burlaga et al., 1981): (i) enhanced magnetic field strength, (ii) smooth rotation of one of the components perpendicular to the Sun – Earth line, and (iii) depressed proton temperature or plasma beta. Sometimes, the term flux rope is used to denote MCs. It is generally believed that the observation of a flux rope structure depends on the viewing angle with respect to the nose of the ICME. In situ plasma and magnetic field measurements are made as the ICME blows past the observing spacecraft. If the spacecraft passes through the nose of the ICME, one observes a flux rope. When the spacecraft deviates significantly from such a trajectory, it may not observe the flux rope structure (see e.g., Marubashi, 1997; Gopalswamy, 2006d), but still observe other plasma and magnetic field signatures of an ICME. For a spacecraft along the Sun-Earth line, this means CMEs originating from the disk center would be observed as MCs while those ejected at larger central meridian distances would be observed as non-MCs. In order to test this hypothesis, we have plotted the solar sources of shock-driving ICMEs in Fig. 18 distinguishing MCs, non-MCs (NC) and "driverless" shocks. The MC sources are generally close to the central meridian, lying with ±30°. The non-MC sources are widely distributed on the disk. The driverless shocks are the extreme cases where no ejecta is observed behind the shock. Of course all the three groups have exceptions. If the exceptions can be explained, the hypothesis can be considered true.
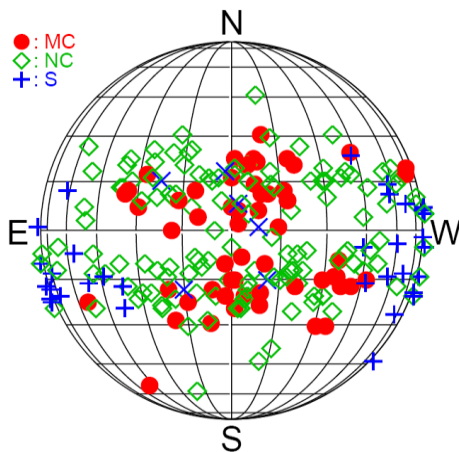

Figure 18. The solar sources of MCs (filled circles), non-MCs (diamonds) and driverless shocks (plus and cross symbols). The crosses denote driverless shocks near the disk center (from Gopalswamy, 2006d).

Let us first look at the driverless shocks. The shocks are known to be due to CMEs originating from large central meridian distances (Gopalswamy et al. 2001c; 2010b). Typically, very fast limb CMEs (limb halos)

result in shocks at 1 AU but the driving ICMEs are missed by the observing spacecraft. However, there are half a dozen driverless shocks originating from close to the disk center. How come these CMEs behave like limb CMEs? Gopalswamy et al. (2009e) found that a large coronal hole was situated near the eruption region such that it deflected the CME away from the Sun – Earth line, making the CMEs behave like limb CMEs. Furthermore, all these disk-center driverless shocks occurred during the declining phase of the solar cycle, when low-latitude coronal holes occur frequently. Thus the disk-center driverless shocks are consistent with the geometrical hypothesis that the ICMEs are missed because they propagate at large angles relative to the Sun – Earth line.

Secondly, the solar sources of two MCs occur at higher latitudes and both are from the rise phase of the solar cycle (see Gopalswamy et al., 2009f). The global solar field is strong and the polar coronal holes are large during the rise phase. One can envision a scenario similar to the low-latitude coronal hole deflection, such that the higher-latitude CMEs are pushed toward the equator (see, e.g. Gopalswamy and Thompson, 2000). Similarly, one can think of the three large-CMD MCs to have some deflection toward the Sun – Earth line. It is also possible that the source identification may be incorrect. Finally, one has to explain why there are so many disk-center non-MCs. Two possibilities can be considered. (i) The pre-eruption equilibrium configuration of the active region is such that the CME is ejected non-radially. (ii) The selection criteria for MCs may be too restrictive and the solar wind data for some of the non-MCs may still be fit to flux ropes (Marubashi 2010, private communication). (iii) In some active regions the CMEs are ejected in rapid succession so CMEs interact resulting in trajectory change (Gopalswamy et al., 2001c). (iv)There may be smaller low latitude coronal holes mildly pushing them away from the Sun-Earth line. (v) The ejecta may rotate to aligns itself with the heliospheric current sheet (Yurchyshyn, 2008). We need to explore these possibilities before arriving at a firm conclusion.

One other argument in favor of the idea that all ICMEs have flux rope structure comes from coronal observations. Flux rope formation seems to be a natural consequence of the eruption process (see e.g., Gosling, 1990) in which the sheared field lines in the source region reconnect to produce the flux rope (see Fig. 19 illustrating the eruption geometry, flux rope formation, and the post-eruption flare arcade). The reconnection results in a flux rope ejected into the IP medium and a flare arcade anchored to the Sun. The magnetic flux in the flare ribbons (at the feet of the flare arcade) and the azimuthal flux in the corresponding MCs in the IP medium seem to have good correlation (Qiu et al., 2007). Similarly, the axial flux in MCs seem to be related to the flux in the dimming region observed in coronal images (see e.g., Webb et al., 2000). The main point is that there is no observational difference between the flare configuration in the solar sources of MCs and
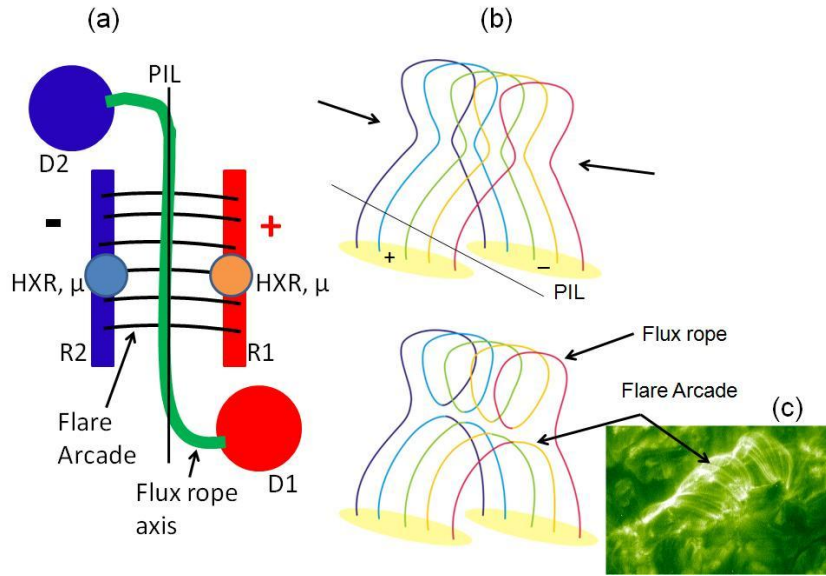
Figure 19. (a) The geometry of a solar eruption including the flare ribbons (R1, R2), the hard X-ray (HXR) and microwave (μ) foot points of the flare on either side of the polarity inversion line (PIL), the flare arcade, and the axis of the flux rope that connects the two dimming regions (D1, D2) located on either side of PIL (adapted from Gopalswamy, 2009). (b) Cartoon reconnection model showing the formation of the flux rope (courtesy: G. Holman). (c) Example of a flare arcade from SOHO/EIT image taken on 2000 September 12.

non-MCs: they have similar neutral lines and flare arcades, so we expect similar flux ropes ejected.

MCs are classified into four types depending on the orientation of the MC axis with respect to the ecliptic (see e.g, Mulligan et al., 1998). If the MC axis is close to the ecliptic plane (low-inclination), the out-of-the ecliptic component (B_z) can change from north to south (NS) in the front to south to north (SN) in the back or SN to NS. MCs are simply identified based on the leading B_z direction and referred to as NS or SN MCs or bipolar MCs. High-inclination MCs have their axes making an angle $> 45^o$ with the ecliptic and are referred to as unipolar MCs because B_z points either to the south or to the north throughout the MC interval. The field rotation is in the Y direction (i.e., in the east-west direction). If B_z points to the north (south) the MC is

said to be of FN (FS) type. The handedness of MCs subdivides each type into two (left and right handed). For example, a NS MC can be NES or NWS depending on the direction of the axial field in the east (E) or west (W) direction (Bothmer and Schwenn, 1994). Similarly, an FN MC can be of ENW or WNE depending on the direction of the east-west component at the leading edge. Figure 20 illustrates the four MC types based on B_z.

The typical magnetic field strength in MCs is ~ 17 nT, which is about three times the solar wind value. The mean speed of MCs at 1 AU is ~478 km/s, very close to the typical slow solar wind speed, even though the corresponding CMEs at the Sun are much faster (~1000 km/s). Depending on the initial speed V, the CME undergoes acceleration due to the interaction with the
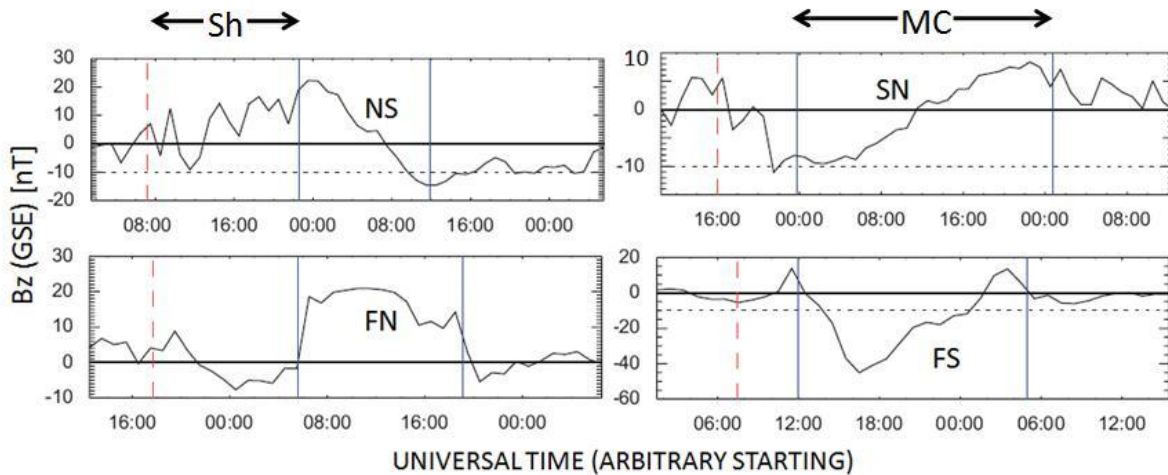

Figure 20. Bipolar (upper panels) and unipolar (lower panel) MCs. All the MCs are shock-driving, so there is a sheath region (Sh) between the MC (between the solid vertical lines and the shock (vertical dashed line) as indicated(Gopalswamy, 2009).

ambient solar wind: $a = -0.0054\,(V - 406)$, where V is in km/s and a is in m/s^2 (Gopalswamy et al., 2001d). For high initial speeds, the relation is quadratic (Gopalswamy, 2009). The average MC duration at 1 AU is ~21 h, which implies a spatial scale of ~0.25 AU for the thickness of the MC (see Lepping and Berdichevsky, 2000; Gopalswamy, 2006d). The relative number of NS and SN MCs show a 22-year solar cycle pattern, apparently decided by the global magnetic field of the Sun. The global field of the Sun reverses during solar maxima, so the predominance switches around this time. Before 2002, the north pole of the Sun had positive polarity and the NS MCs were predominant. After the polarity reversal in 2002, the SN MCs started appearing in larger numbers (see Echer et al., 2005; Gopalswamy, 2008b). The implications of the flux rope structure for its interaction with the magnetosphere will be discussed in a later section.

6. Consequences of CMEs in the Heliosphere

When the CMEs propagate into the heliosphere, they have various consequences. It was already noted that CME-driven shocks can fill a large volume of the heliosphere with energetic particles. The CMEs also arrive at planetary magnetospheres causing magnetic storms. In addition to producing their own particles, CMEs can also deflect energetic particles of galactic origin that enter the heliosphere. When CMEs are close to Earth, they act as a blanket deflecting galactic cosmic rays (GCRs) and hence preventing them from reaching Earth. This phenomenon is known as a Forbush decrease (Forbush, 1938). CMEs continue to propagate beyond Earth into the outer heliosphere and can continue to interact with GCRs contributing to the cosmic ray modulation.

6.1 CMEs and Cosmic Ray Modulation

The primary requirement of GCR modulation is the presence of magnetic irregularities in the heliosphere (Newkirk et al., 1981). CMEs represent one of the possible large-scale magnetic structures that propagate all the way to the edge of the heliosphere. Numerical models of GCR modulation invoke propagating diffusive barriers (PDBs) in the solar wind (see, e.g., McDonald et al., 1981). CMEs are the primary PDB candidates that have the appropriate solar cycle variation. The sunspot number commonly used in correlating GCR intensity with solar activity is only a proxy because sunspots never leave the Sun to interact with GCRs. CMEs originating from the sunspot region are the ones that propagate into the heliosphere. As noted before, high-latitude CMEs during the solar maximum phase are not associated with sunspots. High-latitude CME structures in the heliosphere are especially important because they can directly encounter and deflect GCRs entering the heliosphere along the polar directions. Such situation arises during the A > 0 epochs (when the north pole of the Sun has positive magnetic polarity). During A<0 epochs, only the low-latitude CMEs are more effective (Gopalswamy, 2004). Thus the CME rate is a better index of solar activity than the sunspot number. It must be pointed out that complete data on CMEs exist only since the beginning of cycle 23; more data are needed to confirm the importance of CMEs for GCR modulation.

6.2 CMEs and Geomagnetic Storms

A geomagnetic storm occurs when an IP structure containing southward magnetic field reaches Earth's magnetosphere. The southward field (B_s) merges with the northward field in the magnetopause, resulting in the flow of solar wind energy into the magnetosphere and causing the enhancement of the ring current. The storm mechanism was elucidated by Dungey (1961). The CME connection to geomagnetic storms arises from the fact that CMEs contain B_s either in the flux rope part or in the sheath part if they drive a shock. Statistical studies have shown that the strength of a geomagnetic storm, measured using the *Dst* index (hourly average of the terrestrial low-latitude horizontal magnetic field in nT) as a proxy for the ring current, primarily depends on the magnitude of B_s (in nT) and the speed V (km/s) with which the IP structure impacts Earth's magnetosphere:

$$Dst = -0.01\,V\,B_s - 32. \quad\dots\dots\dots\dots\dots\dots\dots(6)$$

Although equation (6) was derived for CMEs that become magnetic clouds in the IP medium Gopalswamy et al. (2008c), it should apply to any IP structure containing B_s. The southward component of the magnetic field in a CME arises from their flux-rope nature and in the sheath region due to field line draping around the flux rope and compression. Figure 21 shows how the MC structure results in geomagnetic storms with various delays with respect to the MC arrival at Earth. For the NS MC, the B_s is in the trailing portion, so the storm occurs in the tail portion with a delay of ~18 h from the MC arrival. For the SN MC, the B_s is in the leading portion, so the storm occurs there delay is only ~4 h). For the FS MC, the B_s is present throughout the MC, so the storm starts promptly upon the arrival of the MC (delay ~9 h). For the FN MC, there is no B_s during the MC interval, so there is no storm. In the FN case, there is a large storm that peaks in the sheath interval because of the B_s in the sheath.

According to equation (6), the ICME speed also influences the intensity of the geomagnetic storm. The ICME speed is related to the CME near the Sun, suitably modified by the interaction with the solar wind. ICMEs tend to approach the speed of the solar wind at 1 AU, but there are many fast CMEs that remain at significantly higher speeds (see Fig. 3 of Gopalswamy 2010b). Fig. 22 shows the distribution of speeds for CMEs producing major geomagnetic storms. The CME speed distribution peaks around 700 km/s and the average speed is nearly 1000 km/s and is similar to that of halo CMEs and CMEs resulting MCs.
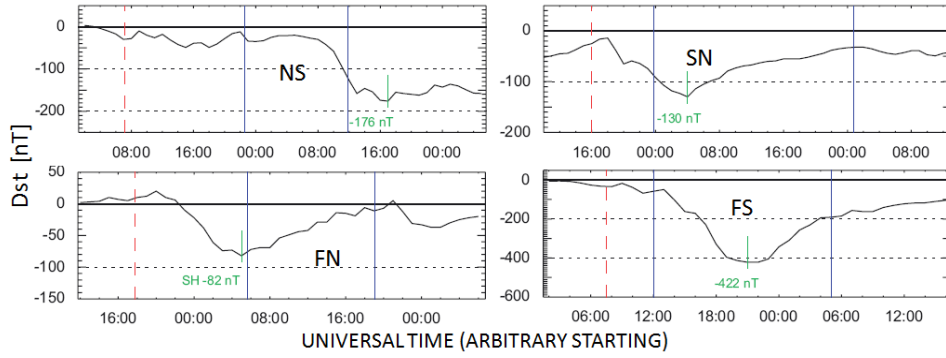
Figure 21. Geomagnetic storms resulting from the four types of MCs described in section 5. The MC is the region between the two vertical lines. The vertical dashed lines mark the shocks (Gopalswamy, 2009).
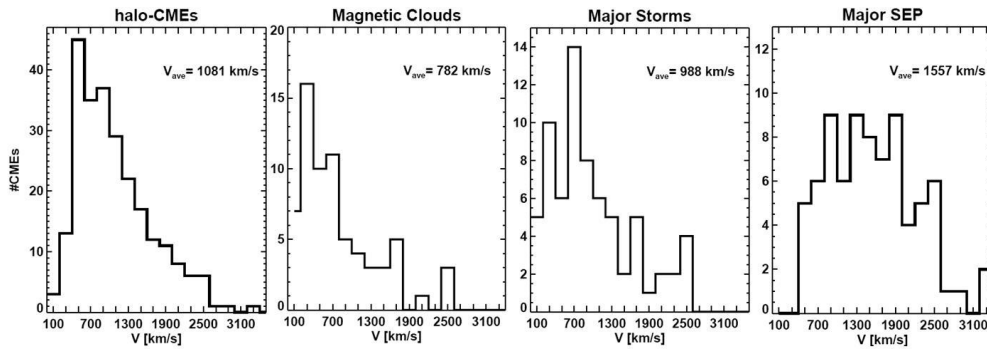

Figure 22. Speed distributions of several CME populations (from left to right): halo CMEs, CMEs resulting in MCs, CMEs producing major geomagnetic storms, and SEP-producing CMEs. The average speeds of the first three are similar, while that of the SEP-producing CMEs is the highest.

CMEs originating close to the disk center are likely to arrive at Earth and cause geomagnetic storm (see Fig. 18). This is the reason why most of the intense geomagnetic storms are caused by MCs (Zhang et al., 2007). This requirement also causes the center-to-limb variation of the geoeffectiveness (the ability to produce a geomagnetic storm) of halo CMEs (Gopalswamy et al., 2007): 75% of halo CMEs with heir solar source close to the disk center are geoeffective. Only 60% of halos originating beyond a CMD of 45° (limb halos) are geoeffective. It appears that the geoeffectiveness of limb halos is primarily due to the B_s in the shock sheath.

Gopalswamy et al. (2008d) examined the IP counterparts for a set of limb halo CMEs (the solar sources of the CMEs were within 30° from the limb). For most of the events, the only IP signature is the shock followed by the sheath because the ICME ejecta are not intercepted by Earth. The lack of ejecta arrival at Earth reduces the probability of limb halos producing a storm, consistent with the center-to-limb variation of geoeffectiveness of halo CMEs (Gopalswamy et al., 2007). When the sheath does contain B_s, the geomagnetic storm immediately follows the shock. The delay time between the CME onset at the Sun and the *Dst* minimum is relatively small in these cases for two reasons: (i) Since limb halos need to be very fast to produce a shock signature along the Sun-Earth line, their earthward speed is typically large. The limb halo speeds ranged from 770 km/s to 3242 km/s with an

average value of 1832 km/s. This is nearly two times the average speed of CMEs producing major (*Dst* < -100 nT) storms, although projection effects play some role in lowering the average speed of these CMEs. (ii) The storms are caused by the shock sheaths, which are the first to arrive at Earth. The delay time ranged from 38 h to 90.5 h, with an average value of 53.3 h. The delay time was ~70 h for storms following disk halos (Gopalswamy et al., 2007). In general, the sheath storms are typically ~3 h ahead of the ejecta arrival, while the ejecta storms are ~11 h behind (Gopalswamy 2008b). Thus the sheath storms are expected to be ~14 h ahead of the ejecta storms.

Figure 23 shows the solar sources of large (Dst ≤ -100 nT) geomagnetic storms from solar cycle 23. The storms are also grouped into three intensity ranges. The solar sources of the largest magnetic storms are clearly close to the central meridian, which enables a head-on collision of the CME with Earth's magnetosphere. The less intense storms have a wider distribution in longitude. The occasional storms with their solar sources close to the limb are the weakest. There is also slight western hemispheric bias of the magnetic storm sources probably because CMEs are deflected eastward due to solar rotation. In summary, fast CMEs originating from close to the disk center cause intense storms provided they contain southward magnetic field component somewhere between the shock and the end of the flux rope.
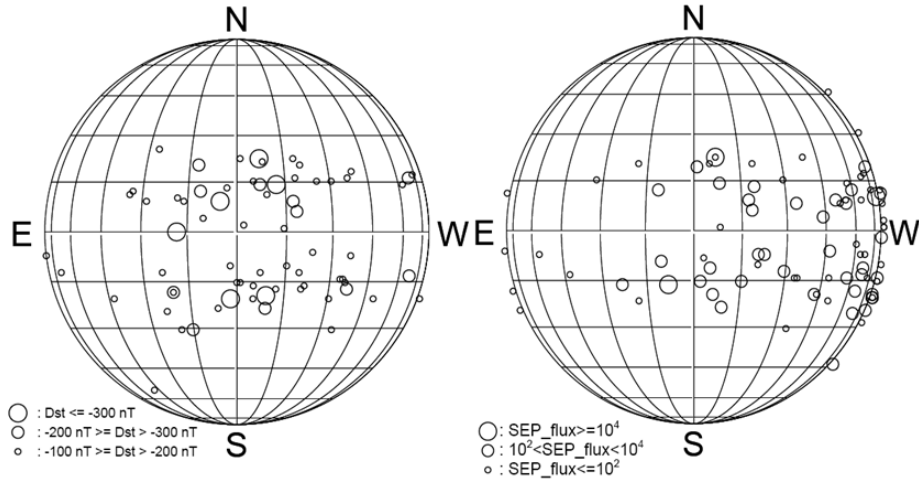
124

Figure 23. Solar source locations of CMEs that produce large SEP events (right) and major (Dst ≤ -100 nT) geomagnetic storms (left).

6.3 CMEs and Solar Energetic Particle Events

Solar energetic particle (SEP) events are so-called because their kinetic energy is much higher than that of the solar wind particles and they acquire the high energy by processes originating from the Sun. The flare reconnection process and the shock acceleration process are thought to be the two primary mechanisms by which particles are energized. The SEP intensity is defined in terms of particle flux units (pfu, 1 pfu = 1 particle cm^{-2} s^{-1} sr^{-1}). SEPs of intensity exceeding 10 pfu in the >10 MeV energy channel are significant because they can affect space technology, astronauts and even the crew and passengers on board airplanes in polar routes. Occasionally the >10 MeV SEP intensity can exceed 10^4 pfu (see Gopalswamy et al., 2005b). Each large SEP event is uniquely associated with an energetic CME (fast and wide). The average sky-plane speed of SEP-associated CMEs is ~1500 km/s, much larger than the average speed (466 km/s, see Fig. 5) of all CMEs. Figure 22 compares the speed distribution of SEP-associated CMEs with three other populations of CMEs. It is clear that all the distributions are skewed, except for the speed distribution of SEP-associated CMEs (symmetric, approximate Gaussian). The average speed of the SEP-associated CMEs is also about 50% higher.

The close similarity among the first three distributions in Fig. 22 is expected because the CMEs originate close to the disk center on the average. Therefore, they are subject to large projection effects. On the other hand, the SEP-associated CMEs originate from the western hemisphere with many events at the limb and even slightly behind the west limb, so they are subject to minimal projection effects (see Fig. 23). The different source positions of CMEs resulting in large SEP events and major geomagnetic storms arise from the geometrical requirements for an observer along the Sun-Earth line. SEPs travel along the Parker spiral field lines of the IP medium, so only particles propagating along the field lines intercepted by Earth can be detected by an observer near Earth. Sources located on the western hemisphere of the Sun are magnetically "well-connected" to Earth. Since CME-driven shocks are of large extent, shock flanks of CMEs originating from outside the well-connected region can connect to the Sun-Earth field lines and cause weak SEP events. On the other hand, the geomagnetic storms are caused by direct plasma impact, so only those CMEs aimed directly at Earth have the highest probability in hitting Earth.

The speed distribution of SEP-producing CMEs is virtually the same (Gopalswamy et al., 2005a) as that of CMEs associated with type II radio bursts that start near the Sun (meter wavelengths) and continue all the way to 1 AU (kilometer wavelengths). There is nearly one-to-one correspondence between the m-km type II bursts originating from the western hemispheric CMEs and the large SEP events (see Gopalswamy et al., 2008a) because the same shock accelerates electrons (observed as type II bursts) and SEPs (detected when they arrive at the detector).

Table 2 compares the average speeds, fraction of full

Table 2. Speed and halo CME fraction for several CME populations compared with SEP-producing CMEs

	Halos	MCs	Non-MCs	Type IIs	Shocks	Storms	SEPs
Speed (km/s)	1089	782	955	1194	966	1007	1557
% Halos	100	59	60	59	54	67	69
% Partial Halos	–	88	90	81	90	91	88
Non-halo Width (°)	–	55	84	83	90	89	48

and partial halos among several special populations of CMEs: CMEs associated with MCs, non-MCs, Type II radio bursts in the IP medium, CMEs associated with IP shocks, CMEs produce large geomagnetic storms, and the SEP-producing CMEs. In addition to being the highest-speed population, there is a high concentration of halo or partial halo CMEs among the SEP-producing CMEs, which is an indicator of their higher energy.

The discussion in sections 4.1 and 4.2 regarding radio quiet CMEs and shocks is also applicable to SEP events because all the major SEP events are associated with type II radio bursts. Figure 24 compares the occurrence rates of major flares (M- and X-class as observed by the GOES satellite in soft X-rays), fast and wide (FW) CMEs (speed ≥ 900 km/s and width ≥ 60°), major SEP events, DH type II bursts, and IP shocks. The numbers are close to one another and vary with the solar cycle in a similar manner, because of the close physical relationship: FW CMEs drive shocks, which accelerate electrons (producing type II radio bursts) and ions (observed in situ as SEP events); the same shocks arrive at 1 AU to be detected by spacecraft. The number of major flares is clearly an exception because it has to be divided by 5 to fit the scale. There are many major flares, which are not associated with CMEs or type II bursts and hence the higher rate for M- and X-class flares. Despite the close correspondence between CMEs and SEP events, several questions remain: CMEs as slow as 500 km/s can produce an SEP event, while a CME as fast as 1500 km/s may not produce an SEP event.

Figure 24 points to three deviations from the CME – shock – SEP connection (1) FW CMEs without type II bursts and SEP events (e.g., the two largest spikes in years 2003 and 2005). These CMEs must be ejected into a medium with high Alfven speeds (exceeding 1500 km/s) such that the CMEs drive either weak shocks or no shocks at all. High Alfven speed can occur when the CME propagates into a tenuous corona and interplanetary medium. Statistical investigations have shown that the Alfven speed can vary by a factor of 4 in the corona (Gopalswamy et al., 2008a,b). (2) DH type II bursts without FW CMEs. A CME may encounter a low Alfven speed when it propagates into a dense medium. At least two very slow CMEs (originating near the limb with speeds of 278 km/s and 358 km/s) are known to be associated with DH type II bursts. These speeds indicate the real cutoff to the speed of shock-driving CMEs due to the lowest possible Alfven speed in the corona. Only two limb CMEs with speeds in the range 700-900 km/s with DH type II bursts had no SEP association. This indicates a higher CME cutoff speed for large SEP events. (3) in-situ shocks not accompanied by DH type II bursts or SEP events. These are the same as the radio quiet shocks discussed in section 4.2.

In addition to the Alfven speed variability, there are other factors that affect the efficiency with which CME-driven shocks accelerate particles. For example, the presence of seed particles in the ambient medium and the presence of preceding wide CMEs seem to result in higher intensity of SEP events (Kahler 2001; Gopalswamy et al., 2001c; 2002; 2004).

Flares are also known accelerators of SEPs and energetic CMEs are associated with major flares, so it is not easy to separate the contributions from the flare and CME in a given SEP event. Since the flare site has a very small angular extent, the SEP events from poorly-connected CMEs are certainly due to shocks. The difficulty is when the CME is well connected to the
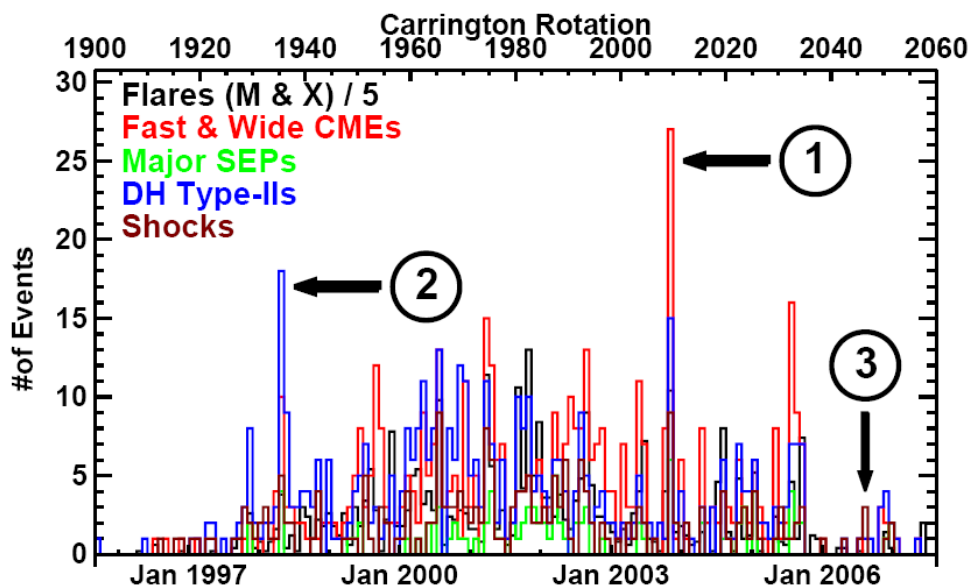

Figure 24. Overall correspondence among energetic events from the Sun as a function of time (1996 to 2008). Some Carrington rotations that deviate from the norm are indicated on the plot: 1. FW CMEs without type II bursts and SEPs, 2. DH type II bursts without FW CMEs, and 3. IP shocks without DH type II bursts and SEPs (from Gopalswamy, 2008a).

observer, in which case one cannot tell whether the SEPs are from the flare site or from the nose of the shock, which is located radially above the flare site, but a few solar radii away (Gopalswamy, 2008a). In extremely rare cases, the early anisotropic peak in the intensity of SEP events with ground level enhancement (GLE) has been interpreted to be due to flare acceleration (McCracken et al., 2008).

A distinct signature associated with most of the SEP events is the low-frequency, long duration type III bursts typically lasting for >20 min (Cane et al., 2002; MacDowall et al., 2009). Assuming that the type III bursts are due to electrons accelerated at the flare reconnection beneath the CMEs, it is possible that ions are also accelerated there. However, Gopalswamy and Mäkelä (2010) reported on a complex, long-duration (~28 min at 1 MHz), low-frequency type III burst associated with a fast and wide CME but not associated with a type II burst or SEP event. They concluded that the presence of a long-duration, low-frequency type III burst is not sufficient for the occurrence of a gradual SEP event. This result is consistent with another study by Cliver and Ling (2009) who did not find the occurrence of a type III bursts to be a characteristic that distinguished between impulsive (due to flare acceleration) and gradual (due to shock acceleration) SEP events. The lack of type II burst and SEP event can be explained under the shock paradigm as a consequence of a marginal shock similar to the radio-quiet shock (as discussed above), while it is difficult to provide such an explanation from the flare paradigm.

7. Summary

The summary of the paper follows. SOHO observations revealed that the CME rate is almost a factor of two larger than previously thought and varied with the solar activity cycle in a complex way (e.g., high-latitude CMEs occurred in great abundance during the solar maximum years). CMEs were found to interact with other CMEs as well as with other large-scale structures (coronal holes), resulting in deflections and additional particle acceleration. STEREO observations have confirmed the three-dimensional nature of CMEs and the shocks surrounding them. The EUV signatures (flare arcades, coronal dimming, filament eruption, and EUV waves) associated with CMEs have become crucial in the identification of solar sources from which CMEs erupt. CMEs with speeds exceeding the characteristic speeds of the corona and the interplanetary medium drive shocks, which produce type II radio bursts. The wavelength range of type II bursts depends on the CME kinetic energy: type II bursts with emission components at all wavelengths (metric to kilometric) are due to CMEs of the highest kinetic energy. Some CMEs, as fast as 1600 km/s do not produce type II bursts, while slow CMEs (400 km/s) occasionally produce type II bursts. These observations can be explained as the variation in the ambient flow speed (solar wind) and the Alfven speed. Not all CME-

driven shocks produce type II bursts because the shocks are likely to be subcritical. The same shocks that produce type II bursts also produce solar energetic particles, whose release near the Sun seems to be delayed with respect to the onset of type II bursts. This may indicate a subtle difference in the acceleration of the ions and ~10 keV electrons needed to produce type II bursts. CMEs slow down or accelerate in the interplanetary medium because of the drag force, which modifies the transit time of CMEs and shocks. Halo CMEs that appear to surround the occulting disk were known before the SOHO era as occasional events. During the SOHO era, they became very prominent because of their ability to impact Earth and producing geomagnetic storms. Halo CMEs are generally more energetic than ordinary CMEs, which means they can produce severe impact on Earth's magnetosphere. Their origin close to the disk center of the Sun ensures direct impact on the magnetosphere, although their internal magnetic structure is crucial in causing storms. The solar sources of CMEs that produce SEP events at Earth, on the other hand, are generally in the western hemisphere because of the magnetic connectivity requirement. Thus, CMEs are very interesting from the point of view of plasma physics as well as practical implications because of their space weather impact.

References

Aguilar-Rodriguez, E., Gopalswamy, N., MacDowall, R., Yashiro, S., and Kaiser, M. I., A Study of the Drift Rate of Type II Radio Bursts at Different Wavelengths, in Proceedings of the Solar Wind 11 / SOHO 16, *Connecting Sun and Heliosphere* (ESA SP-592), 12 - 17 June 2005 Whistler, Canada, eds. B. Fleck, T. H. Zurbuchen, and H. Lacoste, p. 393, 2005

Bastian, T. S., Pick, M., Kerdraon, A., Maia, D., and Vourlidas, A., The Coronal Mass Ejection of 1998 April 20: Direct Imaging at Radio Wavelengths, Astrophys. J. 558, L65, 2001

Bothmer, V. and Schwenn, R. , Eruptive prominences as sources of magnetic clouds in the solar wind, Space Sci. Rev. 70, 215, 1994

Bryant, D. A., Cline, T. L., Desai, U. D., and McDonald, F. B., Explorer 12 Observations of Solar Cosmic Rays and Energetic Storm Particles after the Solar Flare of September 28, 1961, J. Geophys. Res. 67, 4983, 1962

Burlaga, L., Sittler, E., Mariani, F., and Schwenn, R., Magnetic loop behind an interplanetary shock - Voyager, Helios, and IMP 8 observations, J. Geophys. Res. 86, 6673, 1981

Cane, H. V., Sheeley, N. R., Jr., and Howard, R. A., Energetic interplanetary shocks, radio emission, and coronal mass ejections, J. Geophys. Res. 92, 9869, 1987

Cane, H. V., Erickson, W. C., and Prestage, N. P., Solar flares, type III radio bursts, coronal mass ejections, and energetic particles, J. Geophys. Res. 107, 1315, 2002

Chen, J., Howard, R. A., Brueckner, G. E. et al., Evidence of an

Erupting Magnetic Flux Rope: LASCO Coronal Mass Ejection of 1997 April 13, Astrophys. J. 490, L191, 1997

Ciaravella, A., Raymond, J. C., van Ballegooijen, A. et al., Physical Parameters of the 2000 February 11 Coronal Mass Ejection: Ultraviolet Spectra versus White-Light Images, Astrophys. J. 597, 1118, 2003

Cliver, E. W., St. Cyr, O. C., Howard, R. A., and McIntosh, P. S., Rotation-averaged rates of coronal mass ejections and dynamics of polar crown filaments, in Proceedings of the 144th IAU Colloquium, *Solar Coronal Structures*, 14 - 20 September 1993, Tatranska Lomnica, Slovakia, eds. V. Rusin, P. Heinzel and J.-C. Vial, p. 83, 1994

Cliver, E.W., Webb, D. F., and Howard, R. A., On the origin of solar metric type II bursts, Solar Phys. 187, 89, 1999

Cliver, E. W. and Ling, A. G., Low-Frequency Type III Bursts and Solar Energetic Particle Events, Astrophys. J. 690, 598, 2009

Dulk, G. A. and McLean, D. J., Coronal magnetic fields, Solar Phys. 57, 279, 1978

Dungey, J.W., Interplanetary Magnetic Field and the Auroral Zones, Phys. Rev. Lett. 6, 47, 1961

Echer, E., Gonzalez, W. D., and Alves, M. V., On the geomagnetic effects of solar wind interplanetary magnetic structures, Space Weather 4, S06001, 2006

Forbush, S. E., On Cosmic-Ray Effects Associated with Magnetic Storms, J. Geophys. Res. 43, 203, 1938

Gold, T., Discussion of shock waves and rarefied gases, in *Gas Dynamics of Cosmic Clouds*, eds. J. C. van de Hulst and J. M. Burgers, North-Holland Publishing Company, Amsterdam, p. 193, 1955

Gold, T., Magnetic Storms, Space Sci. Rev. 1, 100, 1962

Gopalswamy, N., X-ray and Microwave Signatures of Coronal Mass Ejections, in *Solar Physics with Radio Observations*, eds. T. Bastian, N. Gopalswamy, and K. Shibasaki, NRO Report No. 479, p. 141, 1999

Gopalswamy, N., A Global Picture of CMEs in the Inner Heliosphere, in *The Sun and the Heliosphere as an Integrated System*, eds. G. Poletto and S. T. Suess, Astrophysics and Space Science Library 307, Kluwer Academic Publishers, Dordrecht, p. 201, 2004

Gopalswamy, N., Coronal Mass Ejections of Solar Cycle 23, J. Astrophys. Astron. 27, 243, 2006a

Gopalswamy, N., Consequences of Coronal Mass Ejections in the Heliosphere, Sun and Geosphere 1(2), 5, 2006b

Gopalswamy, N., Coronal Mass Ejections and Type II Radio Bursts, in *Solar Eruptions and Energetic Particles*, eds. N. Gopalswamy, R. A. Mewaldt, and J. Torsti, AGU, Washington, DC, p. 207, 2006c

Gopalswamy, N., Properties of Interplanetary Coronal Mass Ejections, Space Sci. Rev. 124, 145, 2006d

Gopalswamy, N., Type II Radio Emission and Solar Energetic Particle Events, in AIP Conference Proceedings 1039, *Particle Acceleration and Transport in the Heliosphere and Beyond*, p. 196, 2008a

Gopalswamy, N., Solar connections of geoeffective magnetic structures, J. Atmos. Sol.-Terr. Phy. 70, 2078, 2008b

Gopalswamy, N., Coronal mass ejections and space weather, in *Climate and Weather of the Sun-Earth System (CAWSES): Selected Papers from the 2007 Kyoto Symposium*, eds. T. Tsuda, R. Fujii, K. Shibata, and M. A. Geller, Terrapub, Tokyo, p. 77, 2009

Gopalswamy, N., Large-Scale Solar Eruptions, in *Heliophysical Processes*, eds. N. Gopalswamy, S. S. Hasan, and A. Ambastha, Springer, Berlin, p. 53, 2010a

Gopalswamy, N., The CME link to the geomagnetic storms, in Proceedings of IAU Symposium No. 264, *Solar and Stellar Variability: Impact on Earth and Planets*, eds. A. G. Kosovichev, A. H. Andrei, and J.-P. Rozelot, 5, p. 326, 2010b

Gopalswamy, N. and Kundu, M. R., Estimation of the mass of a coronal mass ejection from radio observations, Astrophys. J. 390, L37, 1992

Gopalswamy, N. and Kundu, M. R., Thermal and nonthermal emissions during a coronal mass ejection, Solar Phys., 143, 327, 1993

Gopalswamy, N., Lara, A., Lepping, R. P., Kaiser, M. L., Berdichevsky, D., and St. Cyr, O. C., Interplanetary Acceleration of Coronal Mass Ejections, Geophys. Res. Lett. 27, 145, 2000

Gopalswamy, N. and Thompson, B. J., Early life of coronal mass ejections, J. Atmo. Sol.-Terr. Phy. 62, 1457, 2000

Gopalswamy, N., Yashiro, S., Kaiser, M. L., Howard, R. A. and Bougeret, J.-L., Characteristics of coronal mass ejections associated with long-wavelength type II radio bursts, J. Geophys. Res. 106, 29219, 2001a

Gopalswamy, N., Lara, A., Yashiro, S., Kaiser, M. L., and Howard, R. A., Predicting the 1-AU arrival times of coronal mass ejections, J. Geophys. Res. 106, 29207, 2001b

Gopalswamy, N., Lara, A., Kaiser, M. L., and Bougeret, J.-L., Near-Sun and near-Earth manifestations of solar eruptions, J. Geophys. Res. 106, 25261, 2001c

Gopalswamy, N., Yashiro, S., Michałek, G. et al., Interacting Coronal Mass Ejections and Solar Energetic Particles, Astrophys. J. 572, L103, 2002

Gopalswamy, N., Lara, A., Yashiro, S., Nunes, S., and Howard, R. A., Coronal mass ejection activity during solar cycle 23, In *Solar variability as an input to the Earth's environment* (ESA SP-535), International Solar Cycle Studies (ISCS) Symposium, 23 - 28 June 2003, Tatranská Lomnica, Slovak Republic., ed. A. Wilson, p. 403, 2003a

Gopalswamy, N., Lara, A., Yashiro, S., and Howard, R.A., Coronal Mass Ejections and Solar Polarity Reversal, Astrophys. J. 598, L63, 2003b

Gopalswamy, N., Yashiro, S., Krucker, S., Stenborg, G., and Howard, R. A., Intensity variation of large solar energetic particle events associated with coronal mass ejections, J. Geophys. Res. 109, A12105, 2004

Gopalswamy, N., Aguilar-Rodriguez, E., Yashiro, S. et al., Type II radio bursts and energetic solar eruptions, J. Geophys. Res. 110, A12S07, 2005a.

Gopalswamy, N., Yashiro, S., Liu, Y. et al., Coronal mass ejections and other extreme characteristics of the 2003 October-November solar eruptions, J. Geophys. Res. 110, A09S15, 2005b

Gopalswamy, N., Yashiro, S., and Akiyama, S., Coronal mass ejections and space weather due to extreme events, in *Solar Influence on the Heliosphere and Earth's Environment: Recent Progress and Prospects*, Proceedings of the ILWS Workshop, eds. N. Gopalswamy and A. Bhattacharyya, Quest, Mumbai, p. 79, 2006

Gopalswamy, N., Yashiro, S., and Akiyama, S., Geoeffectiveness of halo coronal mass ejections, J. Geophys. Res. 112, A06112, 2007

Gopalswamy, N., Yashiro, S., Akiyama, S. et al., Coronal Mass Ejections, Type II Radio Bursts, and Solar Energetic Particle Events in the SOHO Era, Ann. Geophys. 26, 3033, 2008a

Gopalswamy, N., Yashiro, S., Xie, H. et al., Radio-Quiet Fast and Wide Coronal Mass Ejections, Astrophys. J. 674, 560, 2008b

Gopalswamy, N., Akiyama, S., Yashiro, S., Michalek, G. and Lepping, R. P., Solar Sources and Geospace Consequences of Interplanetary Magnetic Clouds Observed During Solar Cycle 23, J. Atmos. Sol.-Terr. Phy. 70, 245, 2008c

Gopalswamy, N., Yashiro, S., Xie, H., Akiyama, S., Mäkelä, P., Large Geomagnetic Storms Associated with Limb Halo Coronal Mass Ejections, Advances in Geosciences, Vol. 21, 71, 2008d

Gopalswamy, N., Yashiro, S., Michalek, G., et al., The SOHO/ LASCO CME Catalog, Earth Moon Planets 104, 295, 2009a

Gopalswamy, N., Dal Lago, A., Yashiro, S., and Akiyama, S., The expansion and radial speeds of coronal mass ejections, Central European Astrophysical Bulletin, 33, 115, 2009b

Gopalswamy, N., Akiyama, S., and Yashiro, S., Major solar flares without coronal mass ejections, in Proceedings of IAU Symposium No. 257, *Universal Heliophysical Processes*, eds. N. Gopalswamy and D. F. Webb, 4, p. 283, 2009c

Gopalswamy, N., Thompson, W. T., Davila, J. M. et al., Relation Between Type II Bursts and CMEs Inferred from STEREO Observations, Solar Phys. 259, 227, 2009d

Gopalswamy, N., Mäkelä, P., Xie, H., Akiyama, S., and Yashiro, S., CME interactions with coronal holes and their interplanetary consequences, J. Geophys. Res. 114, A00A22, 2009e

Gopalswamy, N., Akiyama, S., Yashiro, S., Michalek, G., and Lepping, R. P., Erratum to "Solar sources and geospace consequences of interplanetary magnetic clouds observed during solar cycle 23—Paper 1" [J. Atmos. Sol.-Terr. Phys. 70(2-4) (2008) 245-253], J. Atmos. Sol.-Terr. Phys. 71, 1005, 2009f

Gopalswamy, N., Yashiro, S., Michalek, G., Xie, H., Mäkelä, P., Vourlidas, A., and Howard, R. A., A Catalog of Halo Coronal Mass Ejections from SOHO, Sun and Geosphere, 4,, in press, 2009g

Gopalswamy, N., Akiyama, S., Yashiro, S., and Mäkelä, P., Coronal Mass Ejections from Sunspot and Non-Sunspot Regions, in *Magnetic Coupling between the Interior and Atmosphere of the Sun,* Astrophysics and Space Science Proceedings, eds. by S. S. Hasan and R. J. Rutten;., p. 289, 2010a

Gopalswamy, N., Mäkelä, P., Xie, H., Akiyama, S., and Yashiro, S., Solar Sources of ``Driverless'' Interplanetary Shocks, Twelfth International Solar Wind Conference, AIP Conference Proceedings, Volume 1216, pp. 452, 2010b

Gopalswamy, N., Xie, H., Mäkelä, P. et al., Interplanetary Shocks Lacking Type II Radio Bursts, Astrophys. J. 710, 1111, 2010c

Gopalswamy, N. and Mäkelä, P., Long-duration Low-frequency Type III Bursts and Solar Energetic Particle Events, Astrophys. J. 721, L62, 2010

Gosling, J. T., Coronal mass ejections and magnetic flux ropes in interplanetary space, in *Physics of Magnetic Flux Ropes*, eds. C. T. Russell, E. R. Priest and L. C. Lee, Geophys. Monograph Series 58, AGU, Washington, DC, p. 343, 1990

Harrison, R. A., The nature of solar flares associated with coronal mass ejection, Astron. Astrophys., 304, 585, 1995

Harrison, R. A., Bursting the solar bubble: the flare - coronal mass ejection relationship, in *Solar Eruptions and Energetic Particles*, eds. N. Gopalswamy, R. Mewaldt, and J. Torsti, Geophys. Monograph Series 165, AGU, Washington, DC, p. 73, 2006

Howard, R. A., A Historical Perspective on Coronal Mass Ejections, in *Solar Eruptions and Energetic Particles*, eds. N. Gopalswamy, R. Mewaldt, and J. Torsti, Geophys.Monograph Series 165, AGU, Washington, DC, p. 7, 2006

Howard, R. A., Michels, D. J., Sheeley, Jr., N. R., and Koomen, M. J., The observation of a coronal transient directed at earth, Astrophys. J. 263, L101, 1982

Howard, R. A., Sheeley, N. R., Jr., Michels, D. J., Koomen, M. J., Coronal mass ejections - 1979-1981, J. Geophys. Res. 90, 8173, 1985

Hudson, H. S. and Webb, D. F., Soft X-ray signatures of coronal ejections, in *Coronal Mass Ejections*, eds. N. Crooker, J. A. Joselyn, and J. Feynman, Geophys.Monograph Series 99, AGU, Washington, DC, p. 27, 1997

Hudson, H. S. and Cliver, E. W., Observing coronal mass ejections without coronagraphs, J. Geophys. Res. 106, 25199, 2001

Hundhausen, A. J., Sizes and locations of coronal mass ejections – SMM observations from 1980 and 1984-1989, J. Geophys. Res. 98, 13177, 1993

Hundhausen, A, In *The many faces of the sun : a summary of the results from NASA's Solar Maximum Mission*, eds. K. T. Strong, J. L. R. Saba, B. M. Haisch, and J. T. Schmelz, Springer, New York, p. 143 1999

Kahler, S. W., The correlation between solar energetic particle peak intensities and speeds of coronal mass ejections: Effects of ambient particle intensities and energy spectra, J. Geophys. Res. 106, 20947, 2001

Kahler, S. W., Observational properties of coronal mass ejections, in *Solar Eruptions and Energetic Particles*, eds. N. Gopalswamy, R. Mewaldt, and J, Torsti, Geophys. Geophys. Monograph Series 165, AGU, Washington, DC, p. 21, 2006

Kahler, S. W., Hildner, E., and van Hollebeke, M. A. I., Prompt solar proton events and coronal mass ejections, Solar Phys. 57, 429, 1978

Kahler, S. W., Sheeley, N. R., Jr., and Liggett, M., Coronal mass ejections and associated X-ray flare durations , Astrophys. J., 344, 1026, 1989

Kim, I. S. and Alexeyeva, I. V., Magnetic Field Observations of Active Region Prominences , in *Solar Active region Evolution: Comparing Models with Observations*, eds. K. S. Balasubramaniam and G. Simon, ASP Conf. Ser. 68, p. 403, 1994

Koomen, M., Howard, R., Hansen, R., and Hansen, S., The Coronal Transient of 16 June 1972, Solar Phys. 34, 447, 1974

Lepping, R. P. and Berdichevski, D., Interplanetary magnetic clouds: Sources, properties, modeling, and geomagnetic relationship, in Research Signpost, Recent Res. Dev. Geophys. 3, 77, 2000

MacDowall, R. J., Richardson, I. G., Hess, R. A., and Thejappa, G., Re-examining the correlation of complex solar type III radio bursts and solar energetic particles, in Proceedings of IAU Symposium No. 257, *Universal Heliophysical Processes*, eds. N. Gopalswamy and D. F. Webb , 4, p. 335, 2009

Magdalenić, J., Marqué, C., Zhukov, A. N., Vršnak, B., Žic, T., Origin of Coronal Shock Waves Associated with Slow Coronal Mass Ejections, ApJ, 718, 266, 2010

Marubashi, K., Interplanetary magnetic flux ropes and solar filaments, in *Coronal Mass Ejections*, eds. N. Crooker, J. A. Joselyn, and J. Feynman, Geophys. Monograph Series 99, AGU, Washington, DC, p. 147, 1997

McDonald, F. B., Trainor, J. H., Lal, N., van Hollebeke, M. A. I., and Webber, W.R., The Solar Modulation of Galactic Cosmic Rays in the Outer Heliosphere, Astrophys. J. 249, L71, 1981

McCracken, K. G., Moraal, H., and Stoker, P. H., Investigation of the multiple-component structure of the 20 January 2005 cosmic ray ground level enhancement, J. Geophys. Res. 113, A12101, 2008

Moon, Y.-J., Choe, G. S., Wang, H., Park, Y. D., Gopalswamy, N., Yang, G., and Yashiro, S., A Statistical Study of Two Classes of Coronal Mass Ejections, Astrophys. J. 581, 694, 2002.

Moore, R. L., Sterling, A. C., Suess, S. T., The Width of a Solar Coronal Mass Ejection and the Source of the Driving Magnetic Explosion: A Test of the Standard Scenario for CME Production, ApJ, 668, 221, 2007

Mulligan, T., Russell, C.T., and Luhmann, J.G., Solar cycle evolution of the structure of magnetic clouds in the inner heliosphere, Geophys. Res. Lett. 25, 2959, 1998

Neugebauer, M. and Goldstein, B. E., Particle and field signatures of coronal mass ejections in the solar wind, in *Coronal Mass Ejections*, eds. N. Crooker, J. A. Joselyn, and J. Feynman, Geophys. Monograph Series 99, p. 245, 1997

Newkirk, G., Hundhausen, A. J., and Pizzo, V., Solar Cycle Modulation of Galactic Cosmic Rays - Speculation on the Role of Coronal Transients, J. Geophys. Res. 86, 5387, 1981

Ontiveros, V. and Vourlidas, A., Quantitative Measurements of Coronal Mass Ejection-Driven Shocks from LASCO Observations, Astrophys. J. 693, 267, 2009

Payne-Scott, R., Yabsley, D. E., and Bolton, J. G., Relative Times of Arrival of Bursts of Solar Noise on Different Radio Frequencies, Nature, 160, 256, 1947

Qiu, J., Hu, Q., Howard, T. A., and Yurchyshyn, V. B., On the Magnetic Flux Budget in Low-Corona Magnetic Reconnection and Interplanetary Coronal Mass Ejections, Astrophys. J. 659, 758, 2007

Reames, D. V., Particle acceleration at the Sun and in the heliosphere, Space Sci. Rev.,90,413, 1999

Sheeley, N. R., Jr., Howard, R. A., Michels, D. J., Robinson, R. D., Koomen, M. J., and Stewart, R. T., Associations between coronal mass ejections and metric type II bursts, Astrophys. J., 279, 839, 1984

Sheeley, N. R., Jr., Howard, R. A., Michels, D. J., Koomen, M. J., Schwenn, R., Muehlhaeuser, K. H., and Rosenbauer, H, Coronal mass ejections and interplanetary shocks, J. Geophys. Res. 90, 163, 1985

Sheeley, N. R., Jr., Hakala, W. N., and Wang, Y.-M., Detection of coronal mass ejection associated shock waves in the outer corona, J. Geophys. Res. 105, 5081, 2000

Sonett, C. P., Colburn, D. S., Davis, L., Smith, E. J., and Coleman, P. J., Evidence for a Collision-Free Magneto-hydrodynamic Shock in Interplanetary Space, Phys. Rev. Lett. 13, 153, 1964

Thompson, B. J. and Myers, D. C., A Catalog of Coronal "EIT Wave" Transients, Astrophys. J. Suppl. S., 183, 225, 2009

Tokumaru, M., Kojima, M., Fujiki, K., Yamashita, M., and Jackson, B. V., The source and propagation of the interplanetary disturbance associated with the full-halo coronal mass ejection on 28 October 2003, J. Geophys. Res. 112, A05106, 2007

Tousey, R., The Solar Corona, in *Space Research XIII*, eds. M.J. Rycroft and S.K. Runcorn, Akademie-Verlag, Berlin, p. 713, 1973

Uchida, Y., On the Exciters of Type II and Type III Solar Radio Bursts, Publ. Astron. Soc. Jpn. 12, 376, 1960

Veronig, A. M., Temmer, M., and Vršnak, B., High-Cadence Observations of a Global Coronal Wave by STEREO EUVI,

Astrophys. J. 681, L113, 2008

Vourlidas, A., Buzasi, D., Howard, R. A., and Esfandiari, E., Mass
and energy properties of LASCO CMEs , in *Solar variability: from
core to outer frontiers* (ESA SP-506), eds. A. Wilson., 1, ESA
Publications Division, Noordwijk, p. 91, 2002

Vourlidas, A., Wu, S. T., Wang, A. H., Subramanian, P.,
and Howard, R. A., Direct Detection of a Coronal Mass Ejection-
Associated Shock in Large Angle and Spectrometric Coronagraph
Experiment White-Light Images, Astrophys. J. 598, 1392, 2003

Vourlidas, A., Howard, R. A., Esfandiari, E., Patsourakos, S., Yashiro,
S., Michalek, G., Comprehensive Analysis of Coronal Mass
Ejection Mass and Energy Properties Over a Full Solar Cycle,
Astrophys. J. 722, 1522, 2010.

Vršnak, B., Ruzdjak, V., Zlobec, P., and Aurass, H., Ignition of MHD
shocks associated with solar flares, Solar Phys. 158, 331, 1995

Vrnak, B., Ruždjak, D., Sudar, D., and Gopalswamy, N., Kinematics
of coronal mass ejections between 2 and 30 solar radii. What can
be learned about forces governing the eruption?, Astron.
Astrophys. 423, 717, 2004

Wang, C., Du, D. and Richardson, J. D., Characteristics of the
interplanetary coronal mass ejections in the heliosphere between
0.3 and 5.4 AU, J. Geophys. Res. 110, A10107, 2005

Webb, D. F., Lepping, R. P., Burlaga, L. F., et al., The origin and
development of the May 1997 magnetic cloud, J. Geophys. Res.
105, 27251, 2000

Yashiro, S., Gopalswamy, N., Michalek, G. et al., A catalog of white
light coronal mass ejections observed by the SOHO spacecraft, J.
Geophys. Res. 109, A07105, 2004

Yashiro, S., Gopalswamy, N., Akiyama, S., Michalek, G., and
Howard, R. A., Visibility of coronal mass ejections as a function
of flare location and intensity, J. Geophys. Res. 110, A12S05, 2005

Yashiro, S., Michalek, G., Akiyama, S., Gopalswamy, N.,
and Howard, R. A., Spatial Relationship between Solar Flares
and Coronal Mass Ejections, Astrophys. J. 673, 1174, 2008.

Yashiro, S. and Gopalswamy, N., Statistical relationship between
solar flares and coronal mass ejections, in Proceedings of IAU
Symposium No. 257, *Universal Heliophysical Processes*,
eds. N. Gopalswamy and D. F.Webb, 4, p. 233, 2009

Yurchyshyn, V., Relationship between EIT Posteruption Arcades,
Coronal Mass Ejections, the Coronal Neutral Line, and Magnetic
Clouds, Astrophys. J. 675, L49, 2008

Zhang, J., Dere, K. P., Howard, R. A., Kundu, M. R.,
and White, S. M., On the Temporal Relationship between Coronal
Mass Ejections and Flares, Astrophys. J. 559, 452, 2001

Zhang, J., Richardson, I. G., Webb, D. F et al., Solar and interpla-
netary sources of major geomagnetic storms (Dst ≤ -100 nT)
during 1996-2005, J. Geophys. Res. 112, A10102, 2007